1988ApJ...330..695T

THE ASTROPHYSICAL JOURNAL, 330:695–717, 1988 July 15

STARBURST NUCLEUS: GALACTIC-SCALE BIPOLAR FLOW

KOHJI TOMISAKA AND SATORU IKEUCHI
Tokyo Astronomical Observatory, University of Tokyo
Received 1987 February 20; accepted 1987 December 30

ABSTRACT

The galactic scale bipolar outflow from the nucleus of a starburst galaxy is studied. A large wind bubble with the size of a few hundred parsecs at the nuclear region of the starburst galaxy results from the frequent supernova explosions as 0.1 supernovae in a year or more. By two-dimensional hydrodynamical simulation, it is shown that the hot matter heated by supernova explosions interacts with ambient interstellar matter and forms the wind bubble structure, i.e., hot cavity and surrounding cooled shell. The bubble gradually elongates with expansion perpendicularly to the galactic disk. Finally, the shell is broken near the top, and the hot matter in the cavity is collimated and accelerated upwardly. Hot gas goes up to 1–2 kpc above the disk plane. This corresponds to the X-ray emission extending perpendicularly to the galactic disk in M82 and NGC 253. Further, the cooled shell formed near the disk plane seems to correspond to the CO spur extending to the halo region in M82.

Subject headings: galaxies: nuclei — galaxies: structure — galaxies: X-rays — stars: formation — stars: supernovae

I. INTRODUCTION

There has been increasing interest in star formation bursts in many galaxies. Starburst galaxies generally show high star-forming activities in a few hundred parsecs from the center of the galaxies except for IRAS galaxies, where starbursts occur as a whole. These galaxies are observed in different wavelengths such as X-ray, optical, near-IR, far-IR, H I 21 cm, CO 2.6 mm, and radio continuum. To see closely the structure of the interstellar medium (ISM) both in parallel and perpendicular to the galactic disk, edge-on galaxies are suitable. There are two well-known examples of starburst nuclei in nearby galaxies: M82 (NGC 3034) and NGC 253.

Summarizing observational results, we can divide the structure of the ISM at the nuclear region of the galaxy into two parts: disk component and extended component.

The disk component is observed as a disk or a torus with radius ~200 pc in the map of near- and far-IR bands. In the case of M82, the 2.2 μm emission (Rieke *et al.* 1980; Dietz *et al.* 1986), which is considered to be emitted by evolved stellar population, extends to $\sim 17'' \approx 270$ pc (the distance of M82 is assumed 3.25 Mpc; Tammannn and Sandage 1968 here) in the major axis of the galaxy but $\sim 7''$ in the minor axis. Far-IR emission, whose luminosity attains $10^{40.5}$ ergs s^{-1} (Telesco and Harper 1980) and which is considered to be radiated from warm dusts heated by early-type stars just formed by ongoing starburst, shows a similar extent to that in near-IR. Recently, very young supernova remnants are found in VLA maps of M82 and NGC 253. Kronberg, Biermann, and Schwab (1985) found more than 40 compact sources with the size up to 6 pc in M82 (also see Unger *et al.* 1984). Turner and Ho (1985) found nine compact knots in the direction of the major axis of NGC 253. These compact objects trace the IR disk, and they seem to be formed in consequence of ongoing starburst. Furthermore, the brightness of these M82 sources, which have been monitored for 3 yr, decreases rapidly at the rate -1.9% to -9.7% yr^{-1} (Kronberg and Sramek 1985). This suggests that the formation rate of these objects, which we consider the supernova rate, should be as large as 3–5 yr^{-1}.

CO observations give us an overall distribution of molecular matter. Olofsson and Rydbeck (1984), Nakai *et al.* (1987), and Lo *et al.* (1987) have confirmed that CO emission in the central region of M82 has two peaks, and they are interpreted as a "200 pc ring" which extends from $r = 80$–400 pc (Nakai *et al.* 1987). The mass of H_2 in the disk component is estimated by CO observations as $3 \times 10^7\ M_\odot$ (Nakai *et al.* 1987) to $6 \times 10^7\ M_\odot$ (Lo *et al.* 1987). Nakai *et al.* (1987) and Lo *et al.* (1987) also have pointed out that CO emission extends to the halo region of the galaxy (extended component). In their maps of CO column density, we can clearly see a CO ridge or spurlike structure perpendicular to the galactic plane toward the halo. Futher, this ridge emerges from the disk at the distance of ~350 pc from the galactic center. In other words, a CO ridge surrounds the IR disk *cylindrically* up to more than 500 pc from the disk plane.

The extended component is recognized also in X-ray emission. In the case of M82, X-ray emission extends perpendicularly to the disk up to 2–3 kpc (Watson, Stanger, and Griffiths 1984; Kronberg, Biermann, and Schwab 1985). In NGC 253, Fabbiano and Trinchieri (1984) have shown that X-ray emission of the SE side is seen along the minor axis of the galaxy up to ~1.2 kpc from the disk (the distance of NGC 253 is assumed 3.4 Mpc here as indicated by Wynn-Williams *et al.* 1979 and Ulrich 1978). The total luminosities of M82 and NGC 253 amount to, respectively, $L_X \approx 2 \times 10^{40}$ ergs s^{-1} and 6×10^{38} ergs s^{-1} in the *Einstein* HRI band (0.2–4 keV). If the X-ray emission originates in thermal radiation from hot gas with temperature of $\sim 10^7$ K, the electron density and total mass of hot gas in M82 are estimated as $n_e \approx 0.2\ \text{cm}^{-3}$ and $M_X \approx 10^7\ M_\odot$, respectively (Watson, Stanger, and Griffiths 1984). In the case of NGC 253, the total mass of X-ray emitting gas is only $\sim 3 \times 10^5\ M_\odot$ (Fabbiano and Trinchieri 1984). The extended X-ray emission strongly suggests that the upper halo region is shock heated by a burst of supernova explosions in the disk region, which is distinguished as the disk component of starburst nucleus.

The relative distribution of molecular gas and the X-ray emitting gas is suggestive. The spurlike structure seems to consist of a gas which resided in the disk and was pushed aside by the X-ray emitting hot gas, as proposed by Unger *et al.* (1984).

Frequent supernova explosions drive strong winds out of the active nucleus, if the supernova energy is well thermalized. Chevalier and Clegg (1985) have analytically studied the spherically symmetric wind in the case that the energy and the mass are continuously deposited with the rate $\dot{E}$ and $\dot{M}$, respespectively, within the sphere of radius R. They showed that the wind with terminal velocity $\sim(2\text{–}3) \times 10^3[(\dot{E}/10^{43}\ \text{ergs s}^{-1})/(\dot{M}/1\ M_\odot\ \text{yr}^{-1})]^{1/2}$ km s^{-1} blows to $r \gtrsim R$. They stressed that the clouds embedded in the wind outside the sphere ($r \approx 4R$) are compressed and emit efficiently the thermal X-ray. However, some extension of this model is necessary to apply to the realistic starburst nuclei as follows. (1) Deviation from spherical symmetry: hot gas seems to extend more easily into the halo (z-direction) rather than to the disk (radial direction). (2) The energy/mass source is distributed in the disk. (3) The wind interacts with the ambient interstellar matter and forms a wind-bubble structure (Weaver *et al.* 1977).

On the superbubble, which is formed by sequential supernova explosions in an OB association (Tomisaka, Habe, and Ikeuchi 1981), the evolution in a plane-stratified gas distribution has been recently studied by Tomisaka and Ikeuchi (1986). According to their full two-dimensional hydrodynamical simulation, due to the anisotropic density distribution the bubbles become more elongated than those in the homogeneous medium. However, the elongation is seen clearly after the front of the expanding bubble goes over the scale height of density distribution. In the case that the mechanical luminosity emitted from an OB association is small and/or the ambient density is high, the superbubble cannot expand comparable to the scale height during the phase of frequent supernova explosions, which is estimated as roughly several $\times\ 10^7$ yr in an OB association. In this case, a nearly spherical bubble is finally formed. In contrast, an elongated bubble or a funnel is formed in the case with high mechanical luminosity and low ambient density.

In the present paper, by full two-dimensional numerical hydrodynamics we study the evolution of wind bubbles which are formed by freqent supernova explosions after the starburst at the nuclear region of galaxies.

The plan of the present paper is as follows: in § II, the model and numerical procedure are presented. The evolution of the bubble may be much affected by the gas densities of the disk and the supernova explosion rates. We show numerical results for various gas density and supernova rate in § III. Section IV is devoted to the discussion on the comparison with observations.

II. MODEL AND NUMERICAL PROCEDURE

We assume that the star formation and following supernova burst begin abruptly in the interstellar medium which was originally settled in a static equilibrium around a nucleus.

First, we describe the initial gas distribution. Because the total mass within 500 pc from the center of M82 derived from the rotation curve, $(5\text{–}8) \times 10^8\ M_\odot$ (Olofsson and Rydbeck 1984; Nakai *et al.* 1987), is much larger than that of molecular gas $\lesssim 10^8\ M_\odot$, we assume that the gravity of the stellar component is dominant and ignore the self-gravity of gas. Here we tentatively assume that the density of the spherical stellar component obeys the King distribution. Then, in terms of radial distance from the center ϖ, the stellar density $\rho_*(\varpi)$ and its gravitational potential $\phi_*(\varpi)$ are expressed as follows:

$$\rho_*(\varpi) = \frac{\rho_c}{[1 + (\varpi/r_c)^2]^{3/2}}\,, \tag{2.1}$$

$$\phi_*(\varpi) = -4\pi G\rho_c r_c^2 \frac{\ln\{(\varpi/r_c) + [1 + (\varpi/r_c)^2]^{1/2}\}}{\varpi/r_c}\,, \tag{2.2}$$

where ρ_c and r_c represent, respectively, the central density and the core radius, which are determined to reproduce the observed rotation curve along the major axis of the galaxy.

In the present paper, we use the cylindrical coordinate (z, r, ϕ) for numerical simulations and take the z-axis as the rotation axis of the galaxy. We assume the axial symmetry around the z-axis throughout this paper. The gravitational force to the gas is balanced with the centrifugal force and the pressure gradient. Here we assume that on the disk plane ($z = 0$) the centrifugal force is balanced with a part (e^2; $0 \leq e \leq 1$) of the gravitational force. In the case of $e = 1$, the gravity is entirely balanced with the centrifugal force. Assuming that the rotation is uniform in the z-direction, the rotational velocity, v_ϕ, is expressed as

$$v_\phi(r) = \left(e^2 r\,\frac{\partial\phi_*}{\partial r}\right)^{1/2} = e\left(\frac{GM_*}{r_c}\right)^{1/2}\left[\frac{\ln\{r/r_c + [1 + (r/r_c)^2]^{1/2}\}}{r/r_c} - \left[1 + \left(\frac{r}{r_c}\right)^2\right]^{-1/2}\right]^{1/2}, \tag{2.3}$$

with $M_* = 4\pi\rho_c r_c^3$. Then $v_\phi(r)$ indicates the rigid-body rotation ($v_\phi \propto r$) for $r \lesssim r_c$ and approximately flat rotation $[v_\phi \approx v_{\phi\,\text{max}} = 0.54e(GM_*/r_c)^{1/2}]$ for $2r_c \lesssim r \lesssim 5r_c$. To fit the rotation curve along the major axis of M82 by Olofsson and Rydbeck (1984) and Nakai (1986), the parameters in equation (2.3) are determined as $r_c \approx 350$ pc, $v_{\phi\,\text{max}} \approx 60$ km s^{-1}, and $M_* \approx 10^9(v_{\phi\,\text{max}}/60\ \text{km s}^{-1})^2(r_c/350\ \text{pc})e^{-2}\ M_\odot$. Beck *et al.* (1978) have obtained the rotation curve of M82 by using the Ne II 12.8 μm line. They have shown that the rigid-body rotation changes to flat rotation near $8'' \approx 90$ pc from the center. According to this model potential, because the last nondimensional term of equation (2.3) is a slowly varying function of r/r_c for $r_c \lesssim r \lesssim 10r_c$, the effect of varying r_c to the gravitational force is not essential unless M_*/r_c is largely changed. Therefore, as far as we consider the structure larger than 500 pc, there will be small difference between the case $r_c \approx 350$ pc and that of $r_c \approx 90$ pc.

Assuming that the gas is entirely isothermal, its density distribution is given as

$$\rho(r, z) = \rho_0 \exp\left[-\frac{\phi_*(\varpi) - e^2\phi_*(r) - (1 - e^2)\phi_*(0)}{c_s^2}\right], \tag{2.4}$$

where we take the three-dimensional random velocity of clouds as c_s rather than the isothermal sound speed of the interstellar matter. We take $c_s = 30$ km s^{-1} here in accordance with the observation by Olofsson and Rydbeck (1984). This model of density distribution is similar to that in the nucleus of the radio galaxy adopted by Morita (1982).

1988ApJ...330..695T

In Figure 1, we show the density distribution in the case of $r_c = 350$ pc, $v_{\phi\,\max} = 60$ km s^{-1}, $e = 0.9$, and $c_s = 30$ km s^{-1}. On the r-axis, the gas density decreases outwardly, because the $1 - e^2$ part of the gravitational force must be balanced with the pressure gradient. A wall structure open to the top is seen around the z-axis, because of the relatively large radial pressure/density gradient, which is necessary to balance with the excessive centrifugal force at the weaker gravitational field. We can extinguish the wall structure if we take the rotation law as $\partial v_\phi/\partial z < 0$. However, rotating hydrostatic equilibrium with $\partial\Omega/\partial z \neq 0$ is unstable (Tassoul 1978, p. 171). Then we tentatively assume that v_ϕ is constant in the z-direction. Because starburst galaxies often show that they have experienced galaxy-galaxy encounter, the distribution of interstellar gas in the galaxy may be far from hydrostatic distribution in reality. However, it is almost impossible to determine the dynamical state of gas in starburst galaxies definitely just after the ignition of starburst. We take the assumption that starburst occurs in medium settled in a static equilibrium.

Now we proceed to the model for the energy injection. From the distribution of compact nonthermal radio sources, we suppose that the supernova burst occurs within a disk with diameter $d \approx 300$ pc and thickness $h \approx 50$ pc, and we assume that the energy and mass release occurs homogeneously in this disk. Although the supernova explosion rate has been estimated as $r_{\rm SN} \approx 0.3$ SNe yr^{-1} (Rieke *et al.* 1980) to 0.2 SNe yr^{-1} (Kronberg, Biermann, and Schwab 1985), it is not certain. Here we study the range of 0.005–0.2 SNe yr^{-1}. In terms of the ejected energy, $E_{\rm SN}$, and the ejected mass, $M_{\rm ej}$, from a supernova, the averaged mechanical luminosity and mass ejection rate per unit volume become

$$\dot{\epsilon}_{\rm SN} = 3.05 \times 10^{-20}\left(\frac{E_{\rm SN}}{10^{51}\ {\rm ergs}}\right)\left(\frac{r_{\rm SN}}{0.1\ {\rm SNe\ yr^{-1}}}\right)\left(\frac{d}{300\ {\rm pc}}\right)^{-2}\left(\frac{h}{50\ {\rm pc}}\right)^{-1}\ {\rm ergs\ s^{-1}\ cm^{-3}}\ , \tag{2.5}$$

$$\dot{\rho}_{\rm SN} = 6.1 \times 10^{-37}\left(\frac{M_{\rm ej}}{10\ M_\odot}\right)\left(\frac{r_{\rm SN}}{0.1\ {\rm SNe\ yr^{-1}}}\right)\left(\frac{d}{300\ {\rm pc}}\right)^{-2}\left(\frac{h}{50\ {\rm pc}}\right)^{-1}\ {\rm g\ s^{-1}\ cm^{-3}}\ . \tag{2.6}$$

Using the Salpeter's (1955) initial mass function and the stellar lifetime compiled by Tinslay (1972), time average ($\sim 10^7$ yr) of the ejected mass from a star is estimated as 15–30 $M_\odot$ depending upon the upper mass limit of the initial mass function. Therefore, we will show the results for typical two cases of $M_{\rm ej}$, i.e., 10 $M_\odot$ and 30 $M_\odot$. The energy ejected from a supernova explosion is assumed to be 10^{51} ergs.

Assuming the cylindrical symmetry $\partial/\partial\phi = 0$, we use unsteady hydrodynamical equations in two dimensions as basic equations:

$$\frac{\partial \rho}{\partial t} + \frac{\partial}{\partial z}(\rho v_z) + \frac{1}{r}\frac{\partial}{\partial r}(r\rho v_r) = \dot{\rho}_{\rm SN}\ , \tag{2.7}$$

$$\frac{\partial}{\partial t}p_z + \frac{\partial}{\partial z}(p_z v_z) + \frac{1}{r}\frac{\partial}{\partial r}(r p_z v_r) = -\frac{\partial p}{\partial z} - \rho\frac{\partial \phi_*}{\partial z}\ , \tag{2.8}$$

$$\frac{\partial}{\partial t}p_r + \frac{\partial}{\partial z}(p_r v_z) + \frac{1}{r}\frac{\partial}{\partial r}(r p_r v_r) = -\frac{\partial p}{\partial r} - \rho\frac{\partial \phi_*}{\partial r} + \frac{\rho v_\phi^2}{r}\ , \tag{2.9}$$

$$\frac{\partial}{\partial t}p_\phi + \frac{\partial}{\partial z}(p_\phi v_z) + \frac{1}{r}\frac{\partial}{\partial r}(r p_\phi v_r) = -\frac{\rho v_r v_\phi}{r}\ , \tag{2.10}$$

$$\frac{\partial e}{\partial t} + \frac{\partial}{\partial z}[(e + p)v_z] + \frac{1}{r}\frac{\partial}{\partial r}[r(e + p)v_r] = -\frac{\partial \phi_*}{\partial z}p_z - \frac{\partial \phi_*}{\partial r}p_r - \Lambda + \dot{\epsilon}_{\rm SN}\ , \tag{2.11}$$

with

$$e = \frac{p}{\gamma - 1} + \frac{\rho}{2}(v_z^2 + v_r^2 + v_\phi^2)\ , \qquad p_z = \rho v_z\ , \qquad p_r = \rho v_r\ , \qquad p_\phi = \rho v_\phi\ , \tag{2.12}$$

where (p_z, p_r, p_ϕ), e, and Λ represent z-, r-, and ϕ- momentum per unit volume, the thermal plus kinetic energy per unit volume, and the radiative cooling rate by Raymond, Cox, and Smith (1976).

We employ the two-dimensional MacCormack (1971) scheme as a numerical procedure, and the artificial viscosity of the third order (Lapidus 1967) is adopted in order to prevent the numerical instability. This is the same as that adopted by Tomisaka and Ikeuchi (1986). We take two cases of grid spacings, $\Delta z = \Delta r = 10$ pc and $\Delta z = \Delta r = 20$ pc as the need arises. The number of numerical meshes in the z-direction is taken as 144 and in the r-direction as 72. We employ the symmetric boundary condition both on the equatorial plane $z = 0$ and the z-axis $r = 0$. This program was checked and the performance was presented in Tomisaka and Ikeuchi (1986).

Because the supernova rate is so high that the number of supernovae which occur in one time step in each cell is larger than unity, we cannot trace the individual evolution of supernova remnants. Actually, supernova remnants will overlap with each other and lose their individual identity in much shorter time scale than the typical lifetime of starburst ($\sim 10^{7-8}$ yr). The ejected energy is not much dissipated away by mutual interaction of supernova remnants, because supernova remnants interact in their early phase (Ikeuchi 1978), which is realized in the starburst nucleus. Therefore, we simulate the burst of supernova explosions by depositing energy $\dot{\epsilon}_{\rm SN}$ and mass $\dot{\rho}_{\rm SN}$ continuously in the cells which correspond to the disk of starburst.

III. NUMERICAL RESULTS

We calculated 10 cases as summarized in Table 1. Parameters in this simulation are n_0 (density at the center of the disk), $r_{\rm SN}$ (supernova explosion rate), and $M_{\rm ej}$ (ejected mass during a supernova explosion).

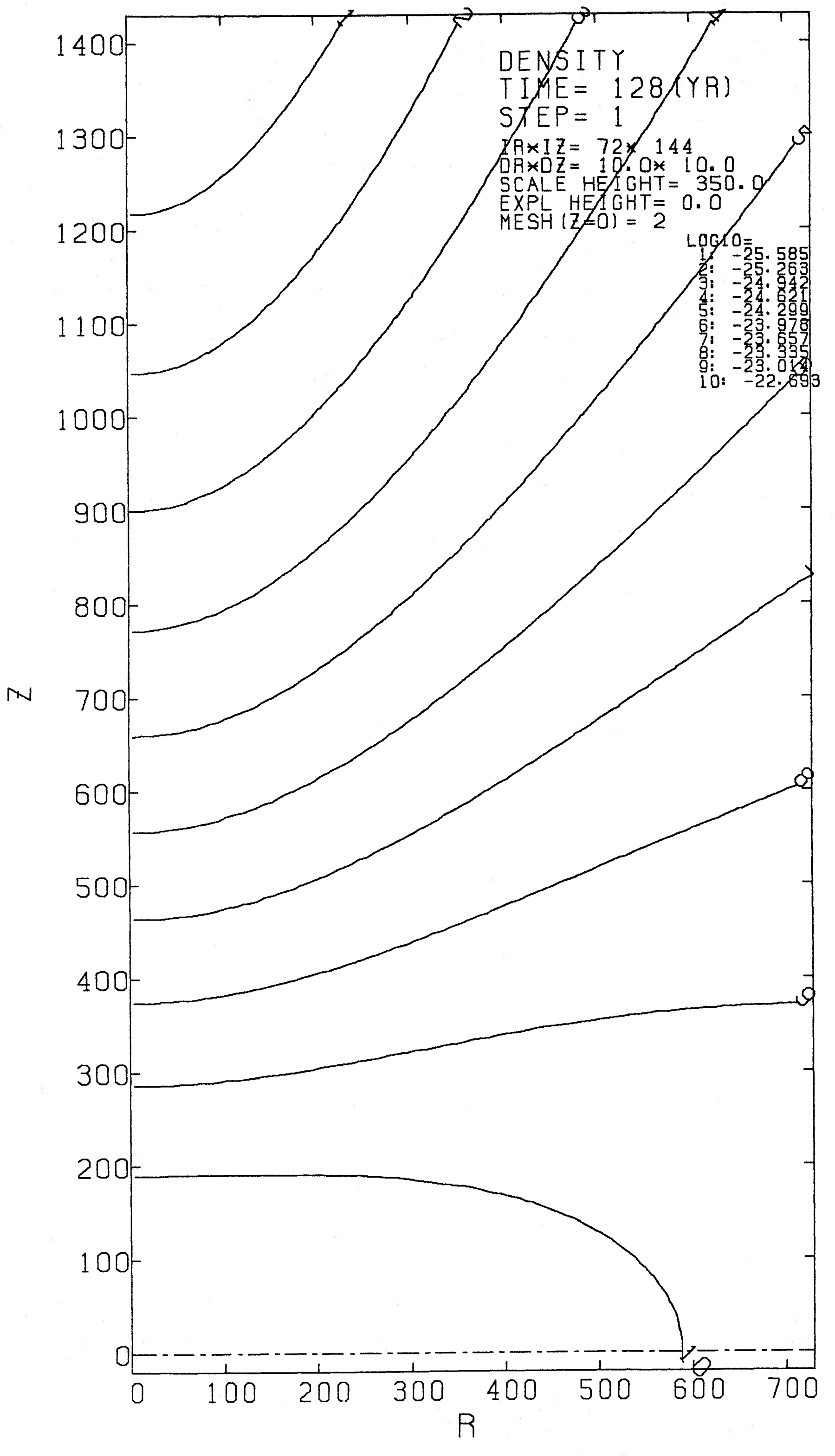

FIG. 1.—Initial gas distribution for the case $r_c = 350$ pc, $c_s = 30$ km s^{-1}, $e = 0.9$, and $n_0 = 20$ cm^{-3}. It shows the density contours in the cross section, where the contour levels (1–10) are written at the upper right part of the panel.

TABLE 1

Adopted Parameters and Calculated X-Ray Luminosity

Case	n_0 (cm^{-3})	Δt[a] (yr)	M_{ej} ($M_\odot$)	L_{HRI} (ergs s^{-1})	Age (Myr)
A	20	10	10	2×10^{40}	4
B	20	10	30	3×10^{40}	4
B2[b]	20	10	30	2×10^{40}	6
C	100	10	30	3×10^{40}	7.5
C2[b]	100	10	30	3×10^{40}	10
D	20	100	30	1×10^{39}	9
E	20	200	30	4×10^{39}	11
F	100	50	30	6×10^{39}	9
P[c]	20	10	30	...	4
P2[b,c]	20	10	30	...	9

[a] Interval of supernova explosions $\equiv r_{\mathrm{SN}}^{-1}$.

[b] In order to pursue the large-scale flow, the mesh size is chosen as $\Delta z = \Delta r = 20$ pc, which is twice as large as other cases.

[c] Plane stratified gas distribution. X-ray luminosity is not calculated.

a) Case A

In Figure 2, we illustrate the evolution of case A ($n_0 = 20$ cm^{-3}, $r_{\mathrm{SN}} = 0.1$ SNe yr^{-1}, and $M_{\mathrm{ej}} = 10\ M_\odot$) at the stages (*a*) $t = 10^6$ yr, (*b*) 2×10^6 yr, and (*c*) 4×10^6 yr after the explosion of the first supernova. At the stage (*a*), the cooled dense shell ($n > 30$ cm^{-3} and $T < 10^4$ K) is formed at $z \approx 180$–260 pc on the z-axis and $r \approx 200$–280 pc on the disk, within which hot rarefied cavity ($T \gtrsim 3\times10^7$ K) spreads. Because the energy injection region extends in the r-direction, the bubble expands preferentially to the radial direction. Since the initial density distribution has a large density gradient to the z-direction, however, the bubble gradually begins to elongate to the z-direction, as seen in Figure 2*b*.

Thermal wind due to the central energy source interacts with the ambient interstellar matter. This is seen well in the sectional views along the z-axis and the r-direction at $z = 0$ of the stage (*b*), as illustrated in Figure 3 by thick lines. In this stage, the wind accelerated from the source is thermalized at an inward-facing shock front standing at a distance of ~200 pc from the center. Because the shock front intersects obliquely with the flow vector, the flow direction turns its direction upward through this oblique shock. The shocked wind pushes ambient medium across the contact discontinuity surface which extends from $(z, r) \approx (350$ pc, 0 pc$)$ to $(0$ pc, 280 pc$)$. Outside of the contact discontinuity, the ambient matter is accumulated and cooled to form the dense shell at 350 pc $\lesssim z \lesssim 460$ pc on the z-axis, and 280 pc $\lesssim r \lesssim 390$ pc on the disk. The structure is isimilar to that of the stellar wind bubble.

Figures 2*c* and 3 (*thin lines*) represent the structure at the age of $t = 4\times10^6$ yr. We can see that the outer shock front expands to ~1 kpc in the z-direction and ~500 pc in the disk. Gas flowing out from the energy injection region becomes isotropic soon, and turns its direction upward at the inward-facing shock.

At this stage, the shell is broken around the z-axis at $r \lesssim 100$ pc and the hot matter in the cavity pushes directly the ambient medium. Różyszka and Tenorio-Tagle (1985) have pointed out that a part of the shell of the bubble which expands into the gas with large density gradient and is accelerated ($\partial \ln z/\partial \ln t > 1$) is broken due to the Rayleigh-Taylor instability. Because before 2×10^6 yr the expansion in the z-direction is decelerated ($\partial \ln z/\partial \ln t < 1$), the density distribution near the contact surface between the shocked low-density wind and the cooled dense shell is stable with respect to the Rayleigh-Taylor instability. It becomes unstable, when the effective gravity, which consists of the gravitational force ($-\partial\phi_*/\partial z$) and the inertia force ($-d^2z/dt^2$), works inwardly ($t \gtrsim 3\times10^6$ yr). This instability plays an important role near the z-axis after $t \gtrsim 3\times10^6$ yr and a part of the shell is broken at $t \sim 4\times10^6$ yr.

The cavity is occupied with the hot matter with $T \approx 10^8$ K and $n \approx 3.5\times10^{-2}$ cm^{-3}, which was originally ejected from supernovae. Comparing the structure at the age $t = 4\times10^6$ yr with that at $t = 2\times10^6$ yr, we can see that the density and pressure decrease to $\frac{1}{3}$. On the other hand, the temperature is kept almost constant as $T \approx 10^8$ K. This is understood as follows: the terminal velocity of the wind from extended source is given as (Chevalier and Clegg 1985)

$$v_w = \left(\frac{2\dot{\epsilon}_{\mathrm{SN}}}{\dot{\rho}_{\mathrm{SN}}}\right)^{1/2} \approx 3.2\times10^3\left(\frac{E_{\mathrm{SN}}}{10^{51}\ \mathrm{ergs}}\right)^{1/2}\left(\frac{M_{\mathrm{ej}}}{10\ M_\odot}\right)^{-1/2}\ \mathrm{km\ s^{-1}}\,. \tag{3.1}$$

If we assume that the wind flows into a standing shock front, the temperature of the shocked wind becomes

$$T_s \approx \frac{3}{16}\frac{\mu H}{k}v_w^2 \approx 1.4\times10^8\left(\frac{\mu}{0.6}\right)\left(\frac{E_{\mathrm{SN}}}{10^{51}\ \mathrm{ergs}}\right)\left(\frac{M_{\mathrm{ej}}}{10\ M_\odot}\right)^{-1}\ \mathrm{K}\,. \tag{3.2}$$

On the other hand, the pressure and density of the shocked wind are well approximated by one-dimensional spherically symmetric solution by Weaver *et al.* (1977) as

$$p \propto L_w^{2/5}t^{-8/5}\,, \tag{3.3}$$

$$\rho \propto \dot{M}L_w^{-3/5}t^{-8/5}\,, \tag{3.4}$$

where L_w denotes the mechanical luminosity of the wind. These indicate the gradual decrease of the pressure and density of the shocked wind.

1988ApJ...330..695T

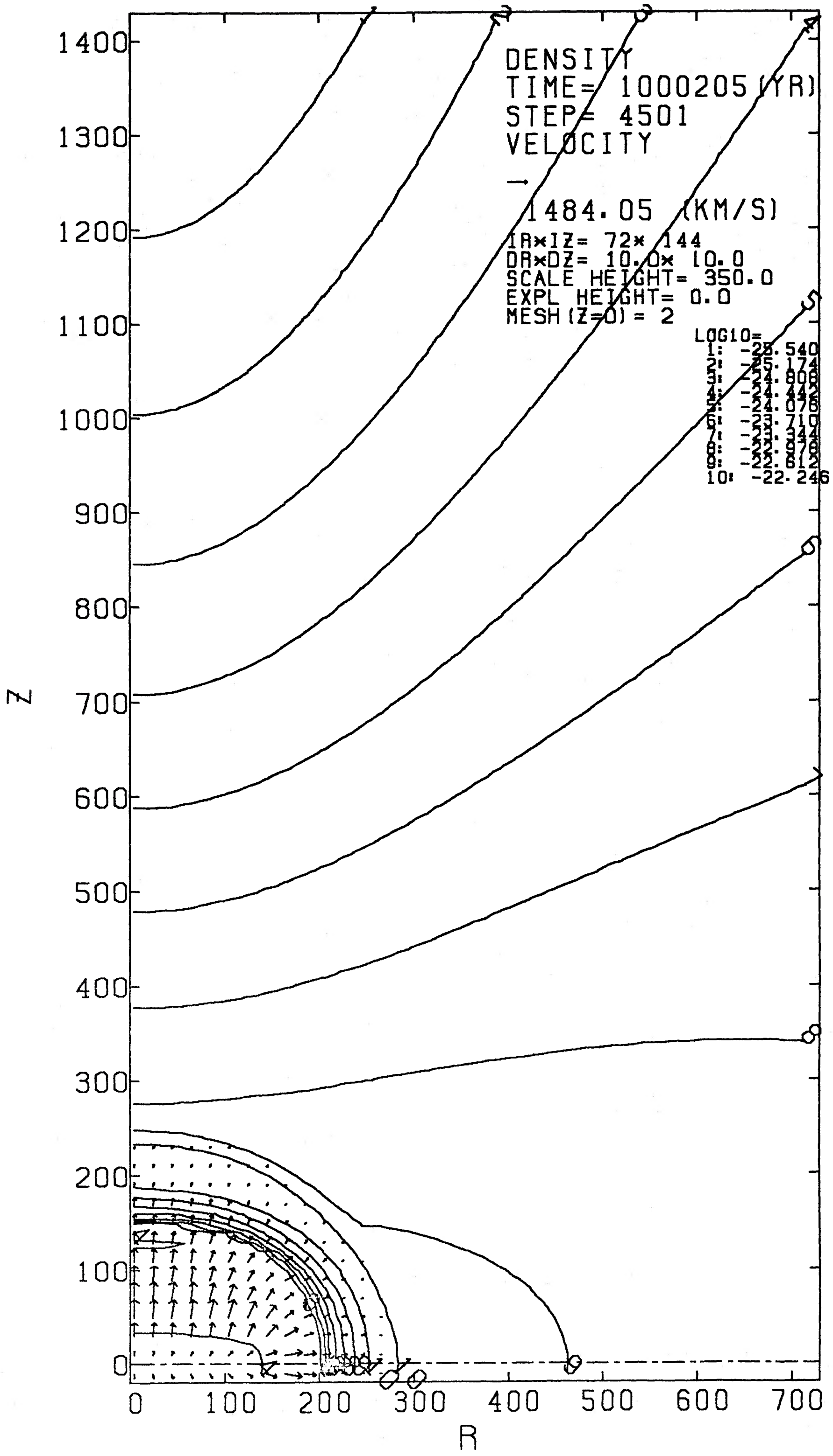

FIG. 2*a*

FIG. 2.—Evolution of the flow in case A. Velocity fields are indicated by arrows, whose length is proportional to the absolute value of velocity. The scale of the arrow is presented in the fifth line at the upper right corner. The flows at (*a*) $t = 1 \times 10^6$ yr, (*b*) $t = 2 \times 10^6$ yr, and (*c*) $t = 4 \times 10^6$ yr are illustrated.

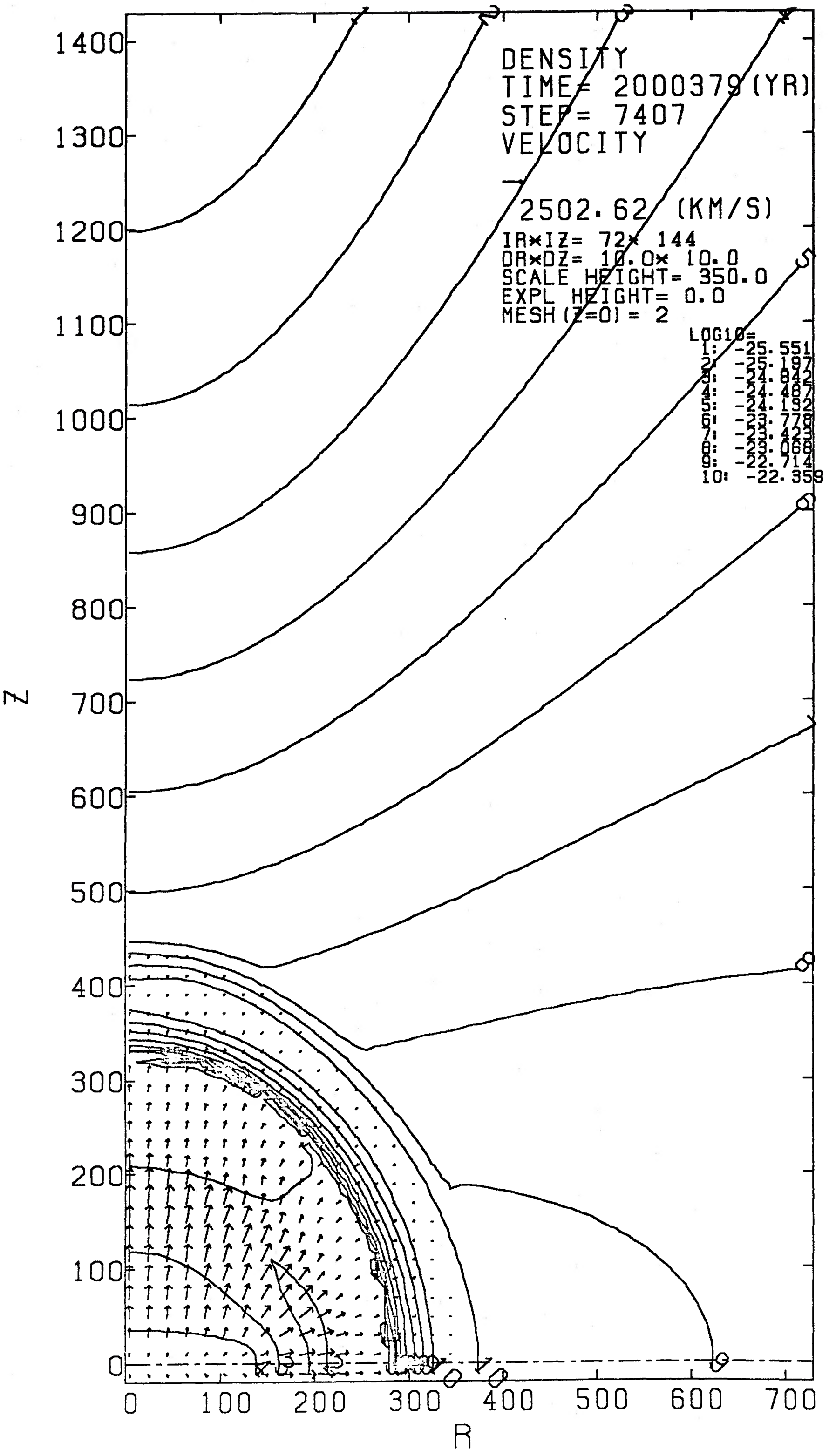
DENSITY
TIME= 2000379 (YR)
STEP= 7407
VELOCITY
→ 2502.62 (KM/S)
IR×IZ= 72× 144
DR×DZ= 10.0× 10.0
SCALE HEIGHT= 350.0
EXPL HEIGHT= 0.0
MESH (Z=0) = 2
LOG10=
1: -25.551
2: -25.197
3: -24.842
4: -24.487
5: -24.132
6: -23.778
7: -23.423
8: -23.068
9: -22.714
10: -22.359
Z
0
100
200
300
400
500
600
700
800
900
1000
1100
1200
1300
1400
R
0
100
200
300
400
500
600
700
1
2
3
4
5
6
7
8
9
0

FIG. 2b

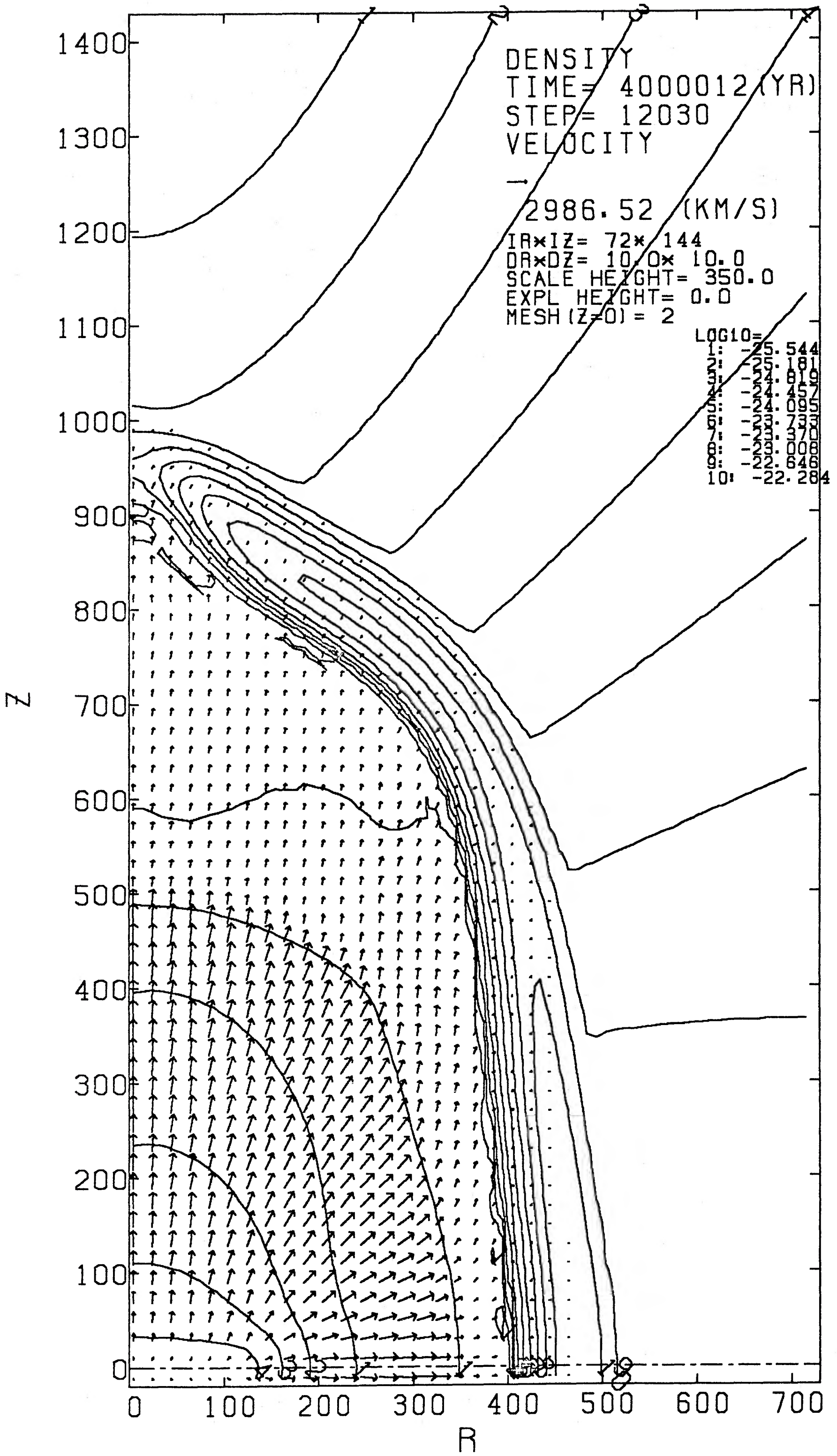
DENSITY
TIME= 4000012 (YR)
STEP= 12030
VELOCITY
→
2986.52 (KM/S)
IR×IZ= 72× 144
DR×DZ= 10.0× 10.0
SCALE HEIGHT= 350.0
EXPL HEIGHT= 0.0
MESH (Z=0) = 2
LOG10=
1: -25.544
2: -25.181
3: -24.819
4: -24.457
5: -24.095
6: -23.733
7: -23.370
8: -23.008
9: -22.646
10: -22.284
Z
1400
1300
1200
1100
1000
900
800
700
600
500
400
300
200
100
0
R
0
100
200
300
400
500
600
700

FIG. 2c

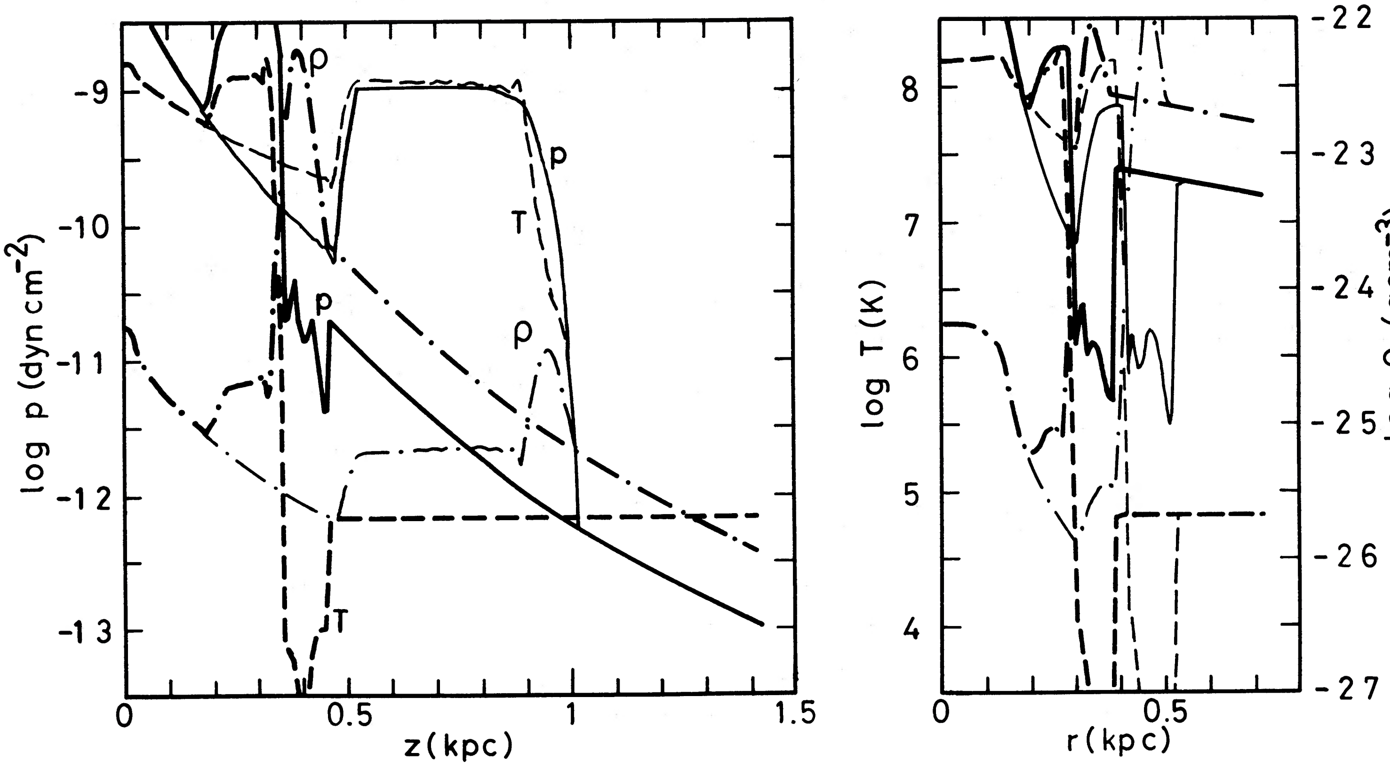

FIG. 3.—The sectional view along the z-axis ($r = 0$) and on the equatorial plane ($z = 0$). We plot physical quantities at $t = 2 \times 10^6$ yr by thick lines and those at $t = 4 \times 10^6$ yr by thin lines.

In case A, we take the ejected mass per one supernova explosion of 10^{51} ergs as 10 $M_\odot$. For other cases, we consider the high-mass ejection case as $M_{\rm ej} = 30\ M_\odot$, where we expect lower temperature in the shocked wind region.

b) The Effect of Mass-Loss Rate (Case B)

Figure 4*a* shows the distribution of density and velocity at the age $t = 4 \times 10^6$ yr of case B. In comparison with Figure 2*c*, the overall structure of the cooled shell and the hot rarefied cavity is similar. However, the flow in the cavity is different. The region of free wind is wider in case B as $z \approx 720$ pc on the z-axis and $r \approx 370$ pc on the disk, while that of case A is $z \approx 500$ pc and $r \approx 340$ pc, respectively. The fact that the inward-facing shock is formed at high altitude affects substantially the structure of the shocked wind region. Although almost all the shocked wind region in case A is subsonic $[(v_r^2 + v_z^2)^{1/2}/(\gamma p/\rho)^{1/2} < 1]$, in case B the subsonic region is restricted to $z \gtrsim 720$ pc near the z-axis and $z \lesssim 300$ pc at $r \gtrsim 340$ pc (near the disk plane), where the wind velocity vector is perpendicular to the shock front.

According to the analytic solution for the spherically symmetric case by Weaver *et al.* (1977), the radius of the inward-facing shock is expressed as

$$r_1 \propto L_w^{1/20} \dot{M}^{1/4} t^{2/5} . \tag{3.5}$$

Compared with case A, the height of the inward-facing shock, $z_1 \sim 3^{1/4}$ times as high as that of case A. This suggests that until this stage ($t \lesssim 4 \times 10^6$ yr) the one-dimensional assumption is marginally valid.

In Figure 4*b*, physical quantities at $t = 4 \times 10^6$ yr along the z-axis and r-axis are plotted. The density in the shocked wind becomes $n \approx 0.09$ cm^{-3}, which is 3 times as high as that of case A, and the temperature is $T \approx 3 \times 10^7$ K, which is one-third as high as that of case A.

After the stage shown in Figure 4, the shell begins to be broken near the z-axis and it is completely broken at $t \approx 4.5 \times 10^6$ yr. Then the shocked wind matter flows directly out to the upper halo region. At that time, since the hot gas is squeezed through a hole, the upward-moving flow seems to be accelerated by the Laval nozzle mechanism. This can be seen in Figure 5, where we plotted the heights of the outward-facing shock with respect to time. As is seen, the shock front is accelerated in this case. Therefore, the expansion of the hot gas to the halo is also accelerated.

In order to follow the evolution after this stage, we extend the simulation area by using a large-sized mesh as $\Delta z = \Delta r = 20$ pc (case B2). If we compare the results of cases B and B2 at the age $t = 4 \times 10^6$ yr, the overall structures of the bubbles agree with each other within 10%. The difference is due to the mingling numerical viscosity. The shell destructuion between 4×10^6 yr and 5×10^6 yr occurs in the same way. Therefore, to study the structure more elongated to the z-direction we appropriately employ the large-sized mesh.

Figure 6*a* shows the structure at the age $t = 6.3 \times 10^6$ yr in case B2. It is found that the cylindrical wall with a radius $r \approx 600$–700 pc is formed below $z \lesssim 1.6$ kpc, through which hot gas is flowing upwardly. On the contrary, above $z \gtrsim 1.6$ kpc the

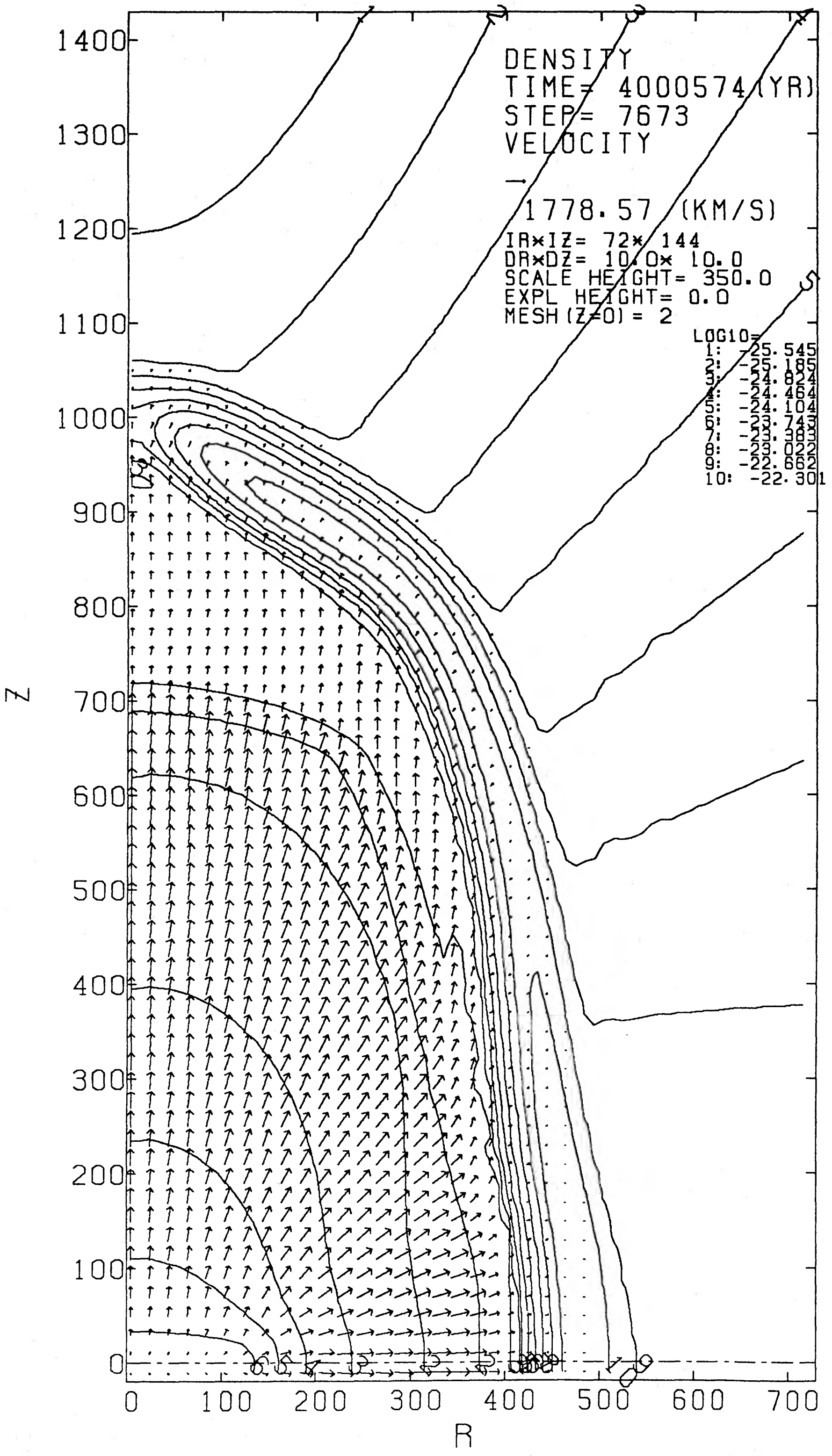

FIG. 4*a*

FIG. 4.—(*a*) Same as in Fig. 2, but for case B at $t = 4 \times 10^6$ yr. (*b*) Same as in Fig. 2, for case B at $t = 4 \times 10^6$ yr.

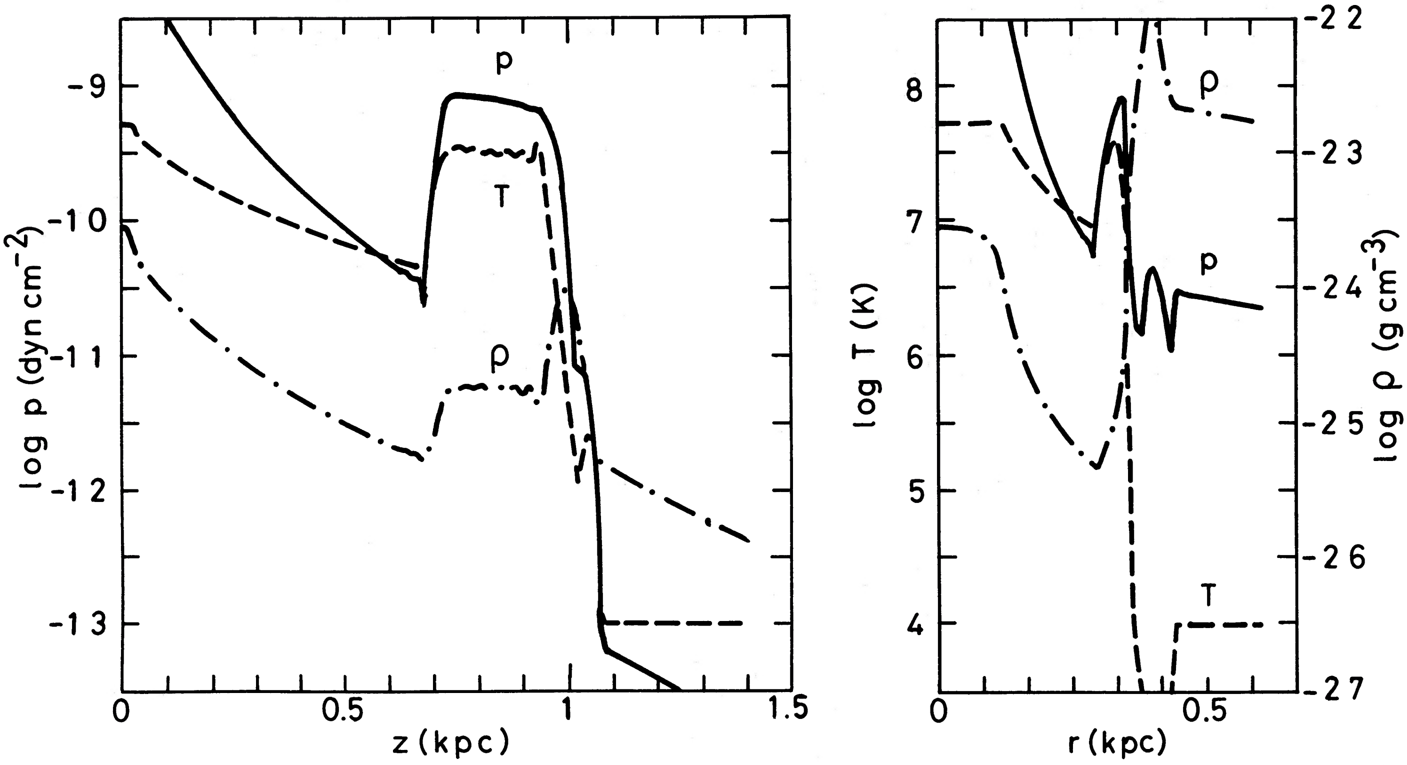

FIG. 4*b*

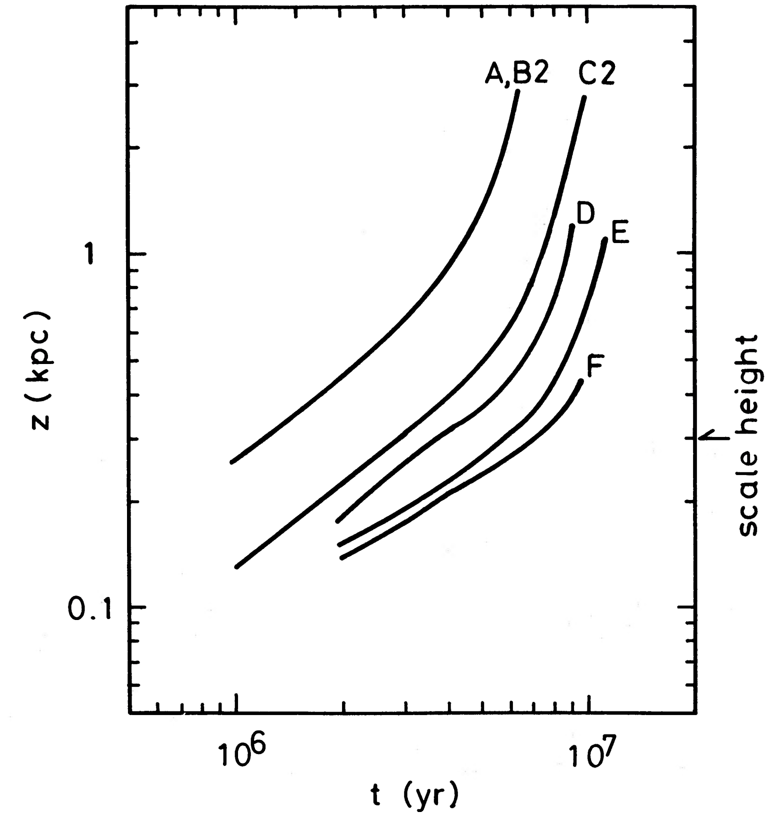

FIG. 5.—Expansion law of the height of the shock front propagating upwardly

1988ApJ...330..695T

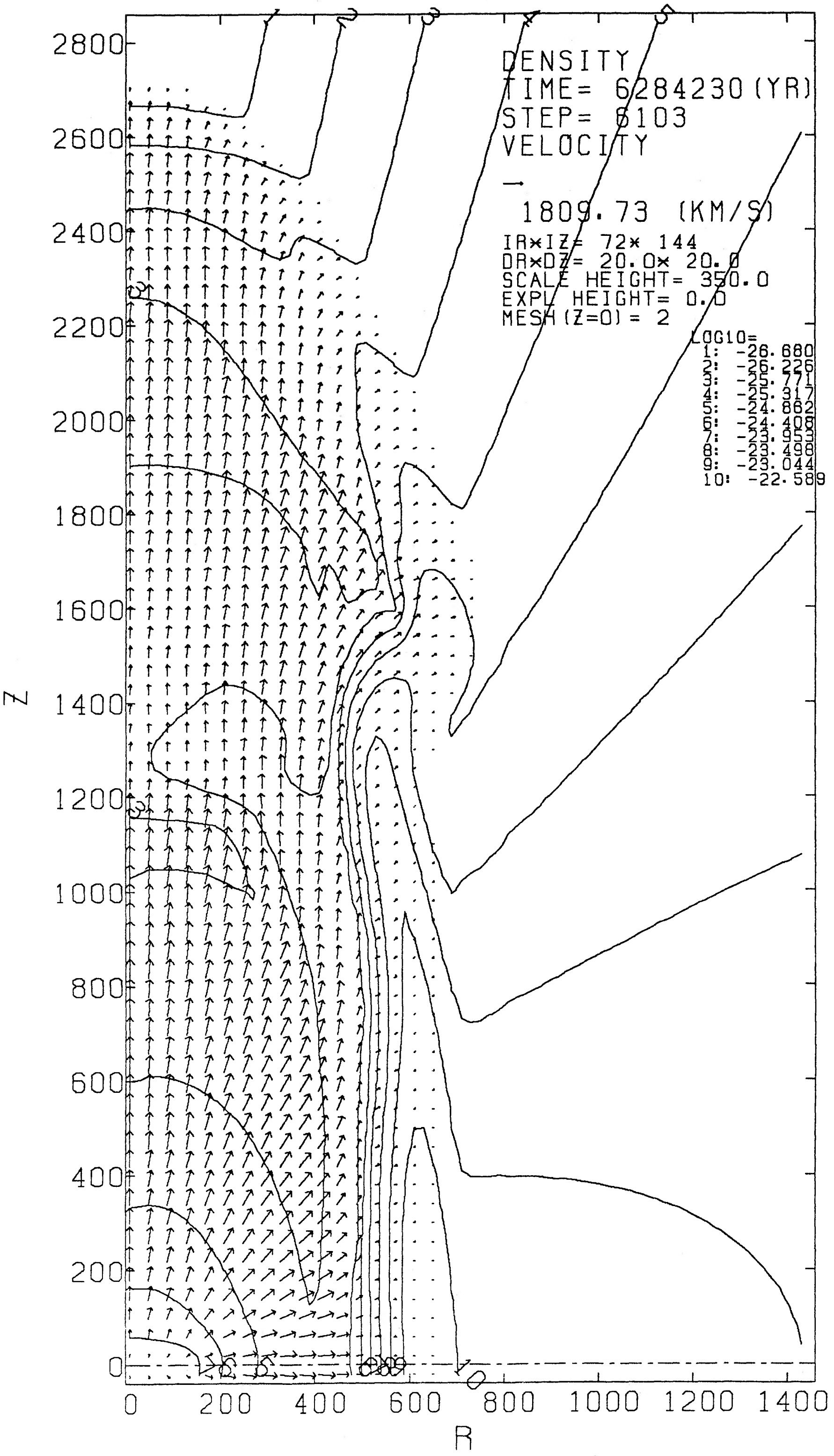

FIG. 6*a*

FIG. 6.—(*a*) Same as in Fig. 2, but for case B2 at $t = 6.3 \times 10^6$ yr. In case B2, meshes with large size are used in order to investigate wider region. (*b*) Same as in Fig. 3, but for case B2 at $t = 6.3 \times 10^6$ yr.

1988ApJ...330..695T

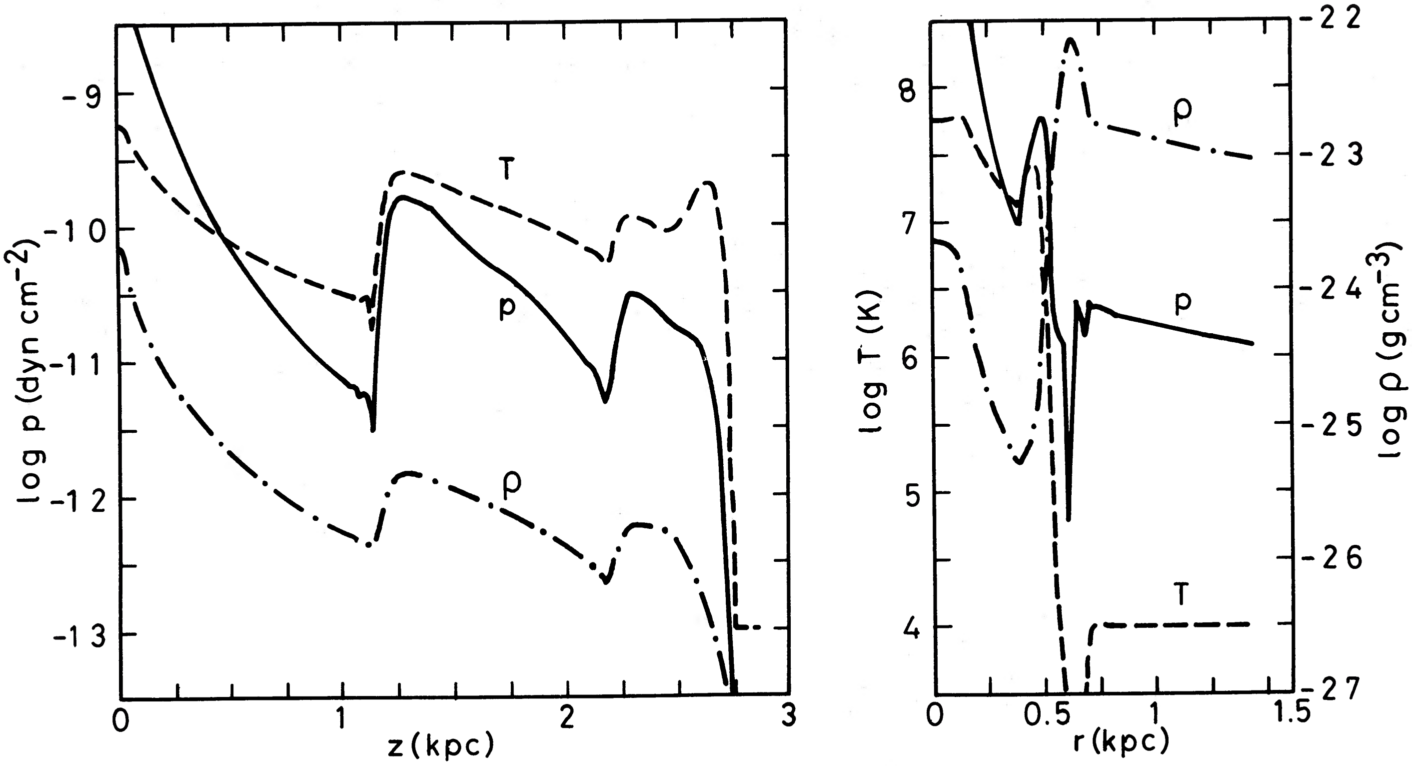

FIG. 6b

dense wall is not formed and the hot gas pushes directly the ambient matter. Such a cylindrical wall and upward hot gas flow in it (like a chimney) are also seen in the superbubble formed by sequential supernova explosions in an OB association (Tomisaka and Ikeuchi 1986). In Figure 6*a*, we can trace the first inward-facing shock from $(z, r) \approx$ (1.2 kpc, 0 pc) to (0 pc, 400 pc), whose location is almost identical with the contour line, No. 4. Although the flow is decelerated at the shock, the postshock flow is reaccelerated due to the compression of ambient medium, and it suffers deceleration once more at the second inward-facing shock, which runs from $(z\ r) \approx$ (2.2 kpc, 0 pc) along the contour line, No. 3. The interface between the reshocked wind material and the ambient matter is located at $z \approx 2.5$ kpc. The cross-sectional view along the z-axis shown in Figure 6*b* clearly shows such structure. This resembles the formation of the Mach disks in the collimated flow (Norman, Winkler, and Smarr 1983). At the stage $t \approx 6.3 \times 10^6$ yr, the temperature in the hot cavity is estimated as $T \sim 10^{7.0 \pm 0.5}$ K, and the density is $n \sim 10^{-2.0 \pm 0.5}$ cm^{-3} at $z \gtrsim 1$ kpc and $10^{-2}(z/1 \text{ kpc})^{-2}$ cm^{-3} at $z \lesssim 1$ kpc.

c) The Effect of Density Distribution (*Case P*)

Since the density on the z-axis is minimum at a fixed z, the outflow may be collimated to the z-axis partly due to this artificial density distribution. To see this clearly, we investigate the case with a special density distribution, i.e., plane-stratified density distribution which only has the density gradient in the z-direction as $\rho = \rho\ (r = 0,\ z)$ using equation (2.4) and $v_\phi = 0$. The gravitational potential is virtually taken to counterbalance the pressure gradient force as $\partial \phi_* / \partial z = -(c_s^2/\rho)\partial\rho(r = 0,\ z)/\partial z$. Other parameters are the same as those of case B.

The structure of the bubble for case P at the age of 4×10^6 yr is seen in Figure 7*a*. Comparing this figure with Figure 4*c*, we can distinguish the differences: (1) the vertical size of the bubble is lower, and (2) the shape of the bubble is rounder. These correspond to the fact that the shell expands more radially than case B due to the absence of the "wall." But these differences are not significant, and we conclude that the effect of the "wall" to the collimation is not so important in the phase of Figures 2, 4*a*, and 7*a*.

Futhermore, we present the structure of the flow for case P2 at the age of 9×10^6 yr in Figure 7*b*. The bubble expands to $z \approx 2.4$ kpc, and $r \approx 1$ kpc, and it clearly shows the bipolar structure. In comparison with case B2 (Fig. 6*a*), the bubble expands more radially in $z \approx 800$–1400 pc. Further, the time necessary for the bubble to expand to $z \sim 2.5$ kpc ($\sim 9 \times 10^6$ yr) is 1.5 times longer than that of case B2 ($\sim 5 \times 10^6$ yr). This means that the density distribution like Figure 1 promotes the collimation of a flow. However, it has been shown that the *density stratification in the z-direction* accelerates the expansion in the z-direction and forms the galactic bipolar flow or bipolar bubble.

d) The Effect of Ambient Density (*Case C*)

In case C, we study the effect of the dense ambient matter as $n_0 = 100$ cm^{-3}. Due to the high density near the disk plane, we expect that the bubble cannot expand so large as those in cases A and B, where the central density is taken to be equal to $n_0 = 20$ cm^{-3}.

At the time $t = 4 \times 10^6$ yr, the bubble only expands to $z \approx 450$ pc and $r \approx 370$ pc as in Figure 8*a*. Suppression of expansion due to high density is clearly seen if we compare this figure with Figures 2*c* and 4*a*. The density and temperature in the cavity are,

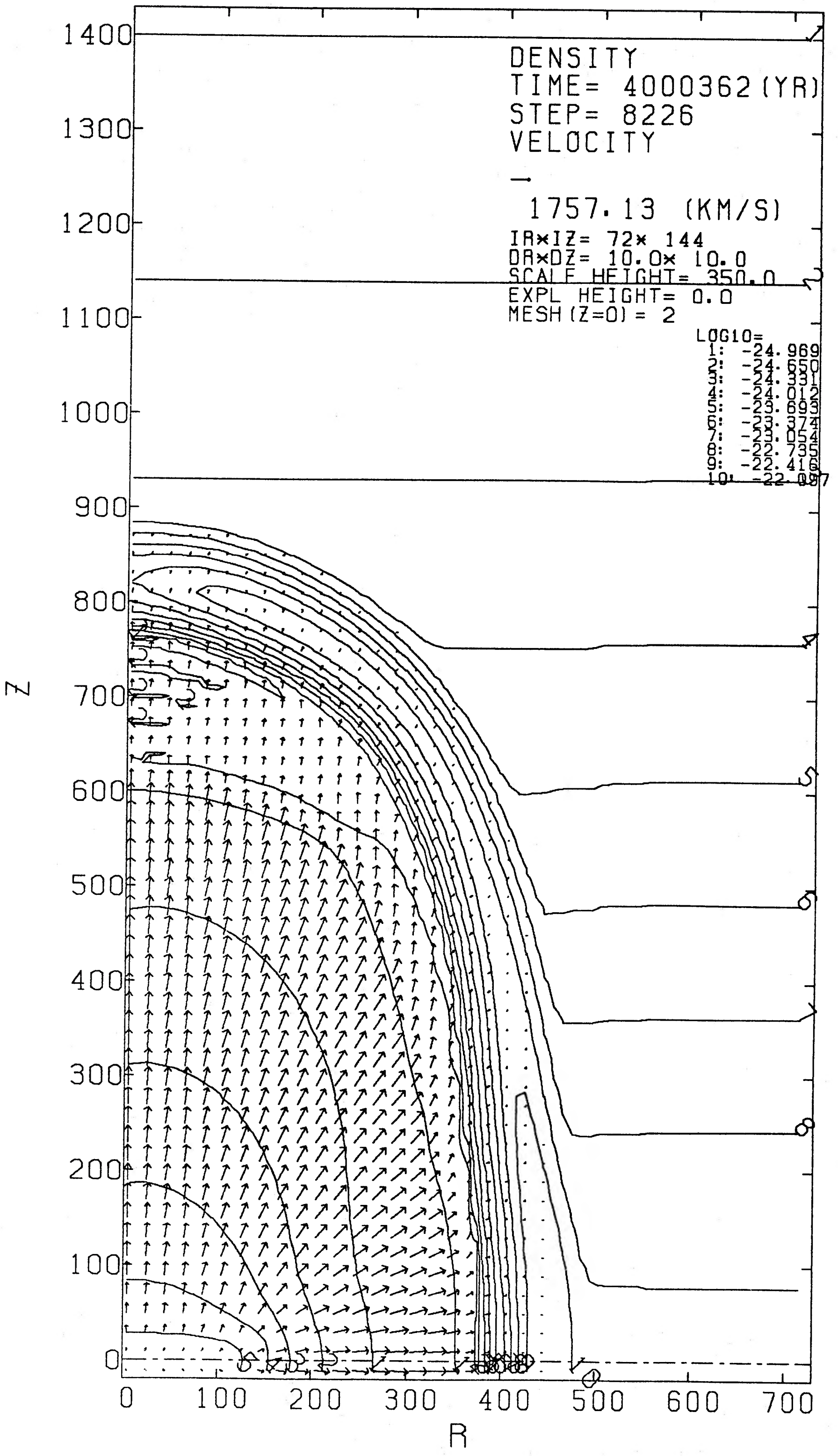

FIG. 7*a*

FIG. 7.—(*a*) Same as in Fig. 2, but for case P at $t = 4 \times 10^6$ yr. In case P, we take the plane-stratified initial density distribution whose density gradient is the same as cases A and B. (*b*) Same as in Fig. 2, but for case P2 at $t = 9 \times 10^6$ yr.

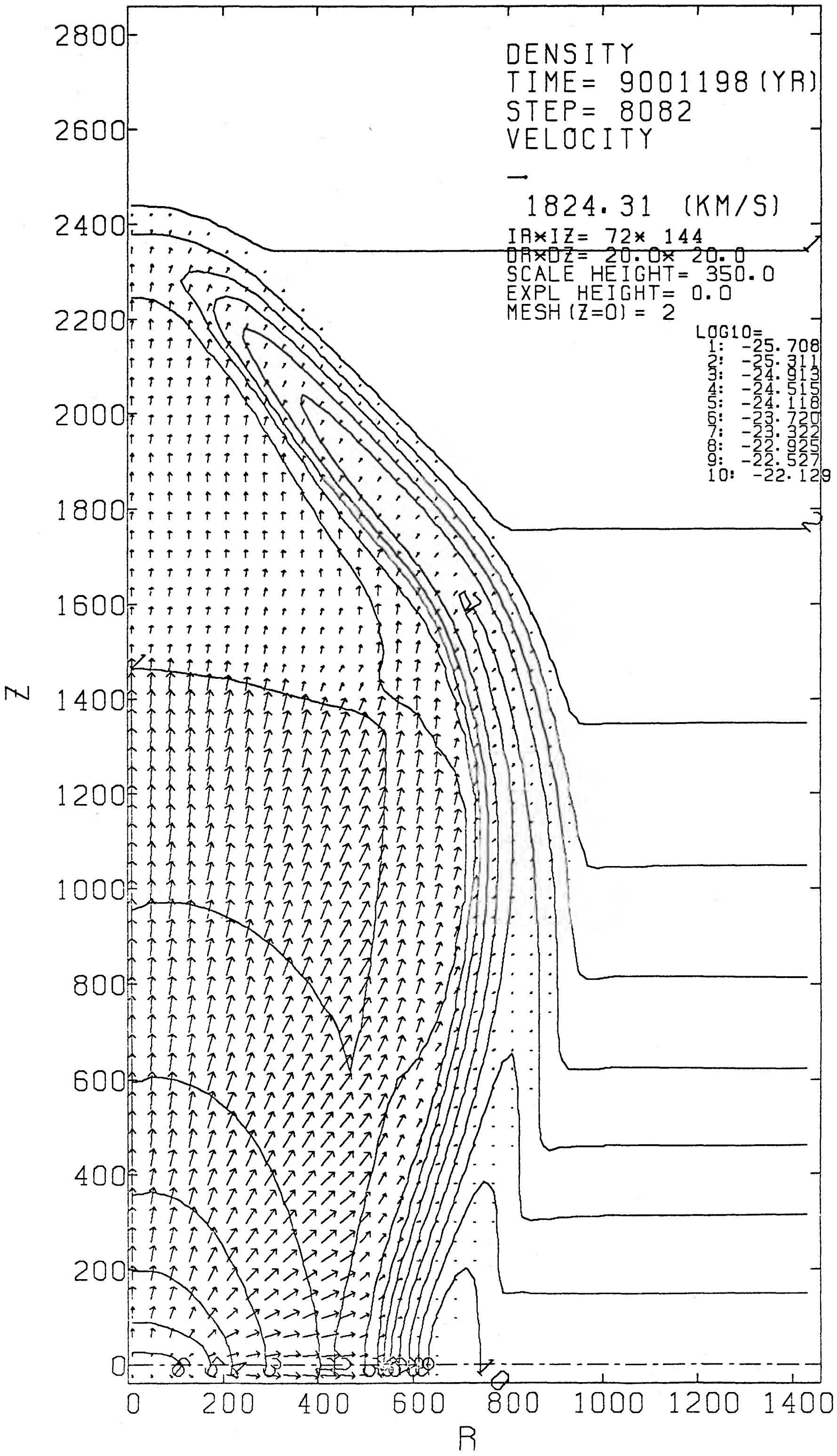
DENSITY
TIME= 9001198 (YR)
STEP= 8082
VELOCITY
1824.31 (KM/S)
IR×IZ= 72× 144
DR×DZ= 20.0× 20.0
SCALE HEIGHT= 350.0
EXPL HEIGHT= 0.0
MESH (Z=0) = 2
LOG10=
1: -25.708
2: -25.311
3: -24.913
4: -24.515
5: -24.118
6: -23.720
7: -23.322
8: -22.925
9: -22.527
10: -22.129
Z
R
0
200
400
600
800
1000
1200
1400
1600
1800
2000
2200
2400
2600
2800

FIG. 7*b*

1988ApJ...330..695T

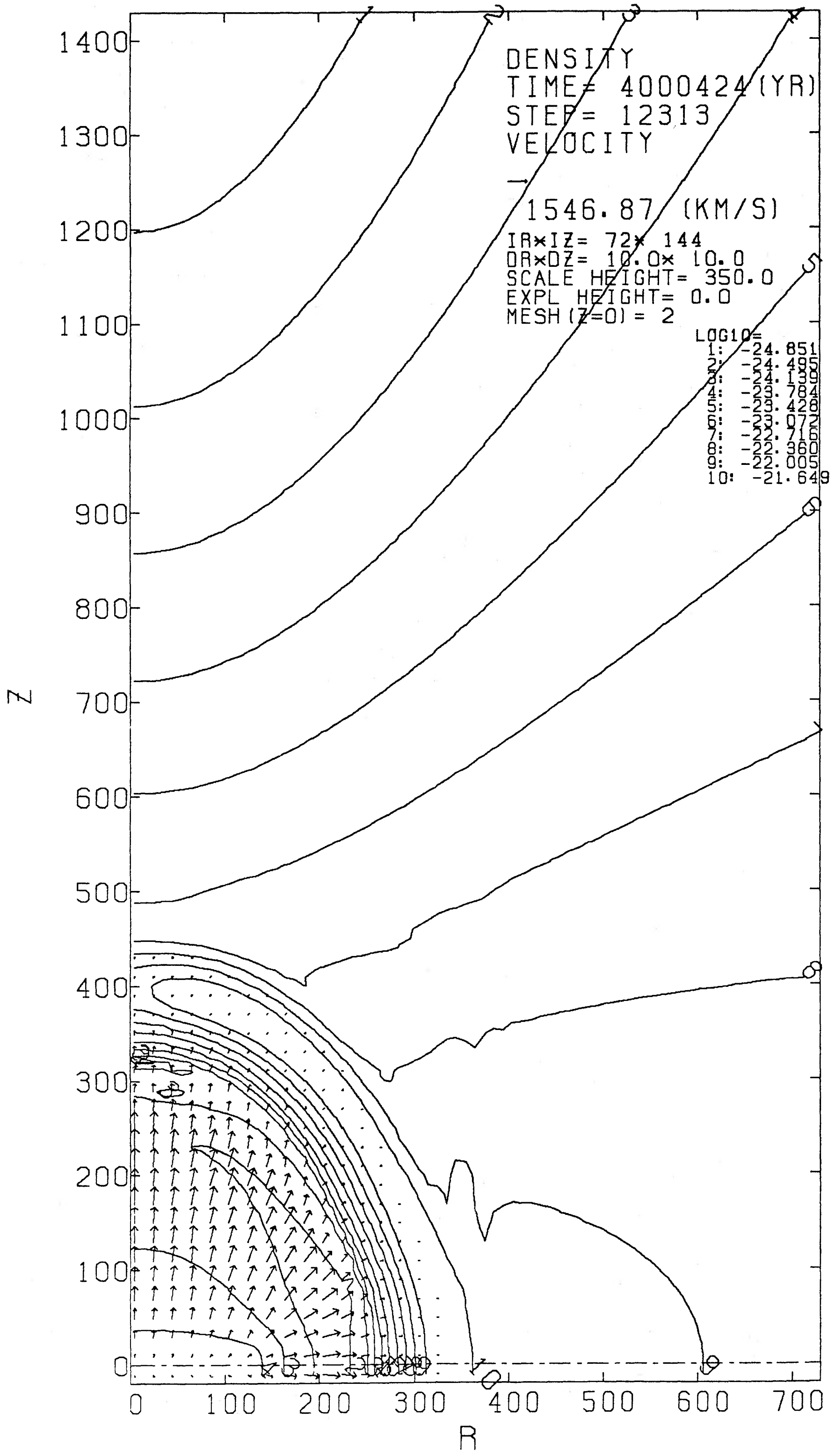

FIG. 8*a*

FIG. 8.—Same as in Fig. 2, but for case C ($n_0 = 100$ cm^{-3}) at (*a*) $t = 4 \times 10^6$ yr, (*b*) $t = 7 \times 10^6$ yr, and (*c*) $t = 10^7$ yr; (*c*) shows the result in case C2

1988ApJ...330..695T

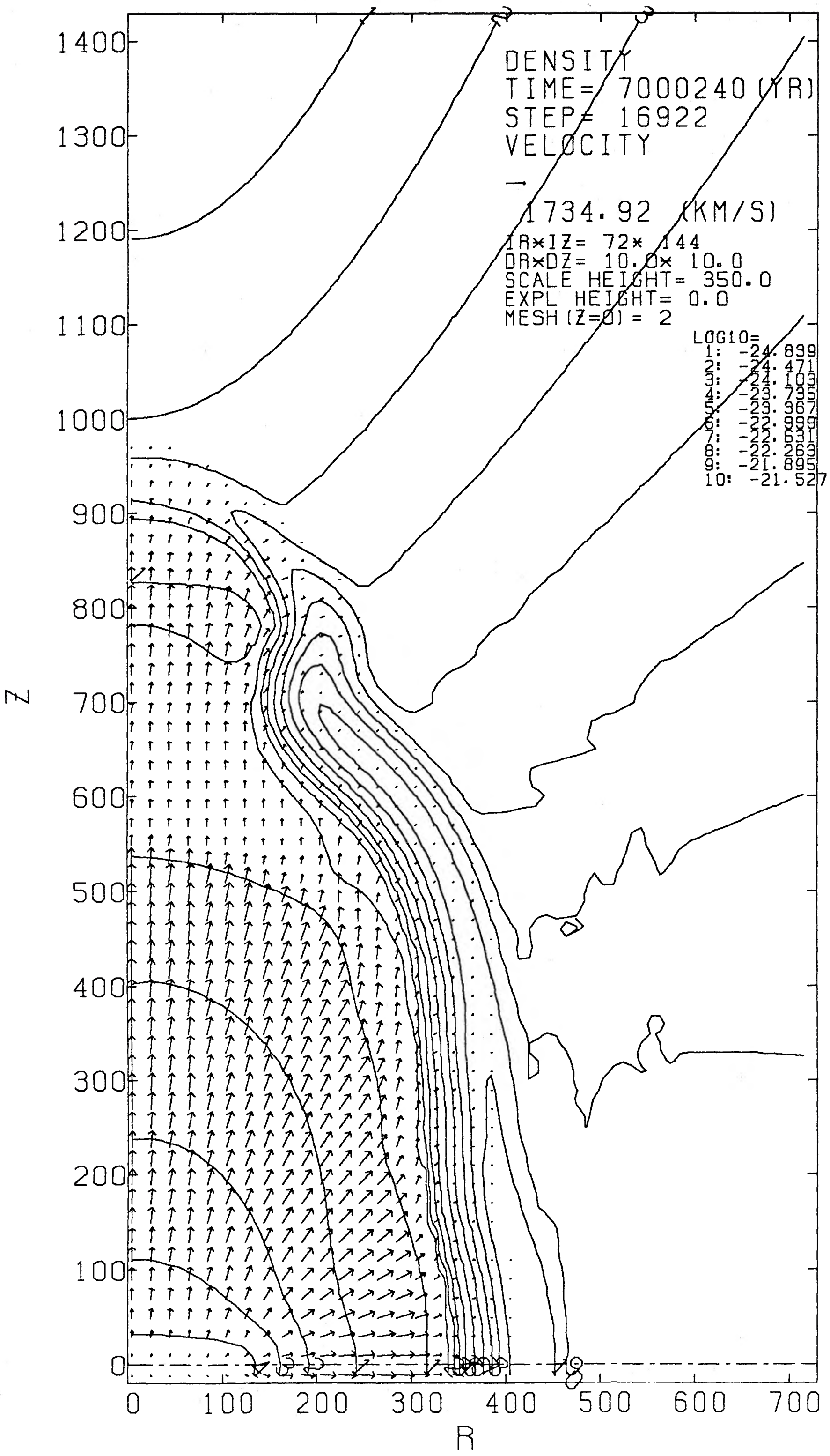

FIG. 8b

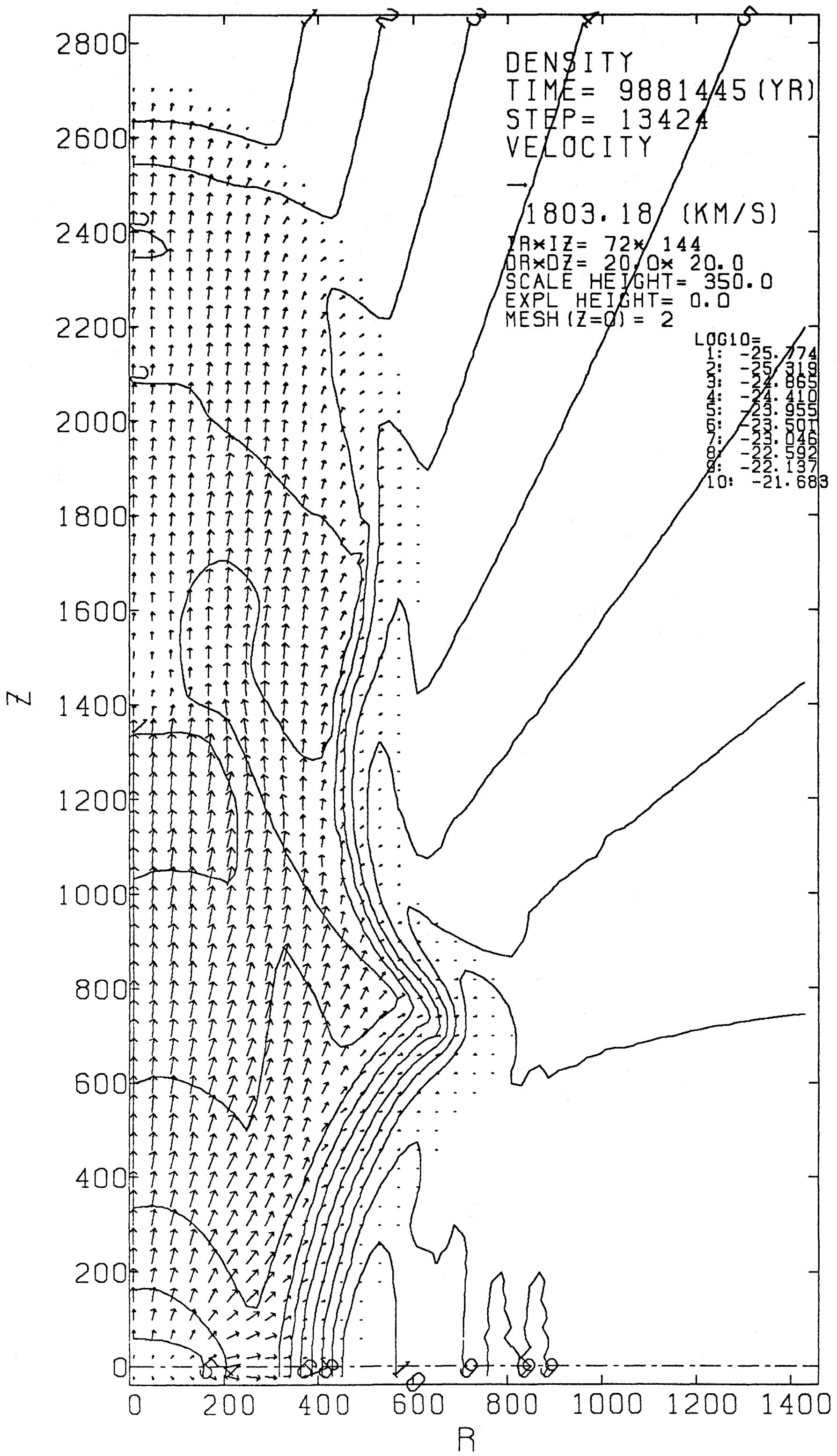
DENSITY
TIME= 9881445 (YR)
STEP= 13424
VELOCITY
→
1803.18 (KM/S)
IR×IZ= 72× 144
DR×DZ= 20.0× 20.0
SCALE HEIGHT= 350.0
EXPL HEIGHT= 0.0
MESH (Z=0) = 2
LOG10=
1: -25.774
2: -25.319
3: -24.865
4: -24.410
5: -23.955
6: -23.501
7: -23.046
8: -22.592
9: -22.137
10: -21.683
Z
0
200
400
600
800
1000
1200
1400
1600
1800
2000
2200
2400
2600
2800
R
0
200
400
600
800
1000
1200
1400

FIG. 8c

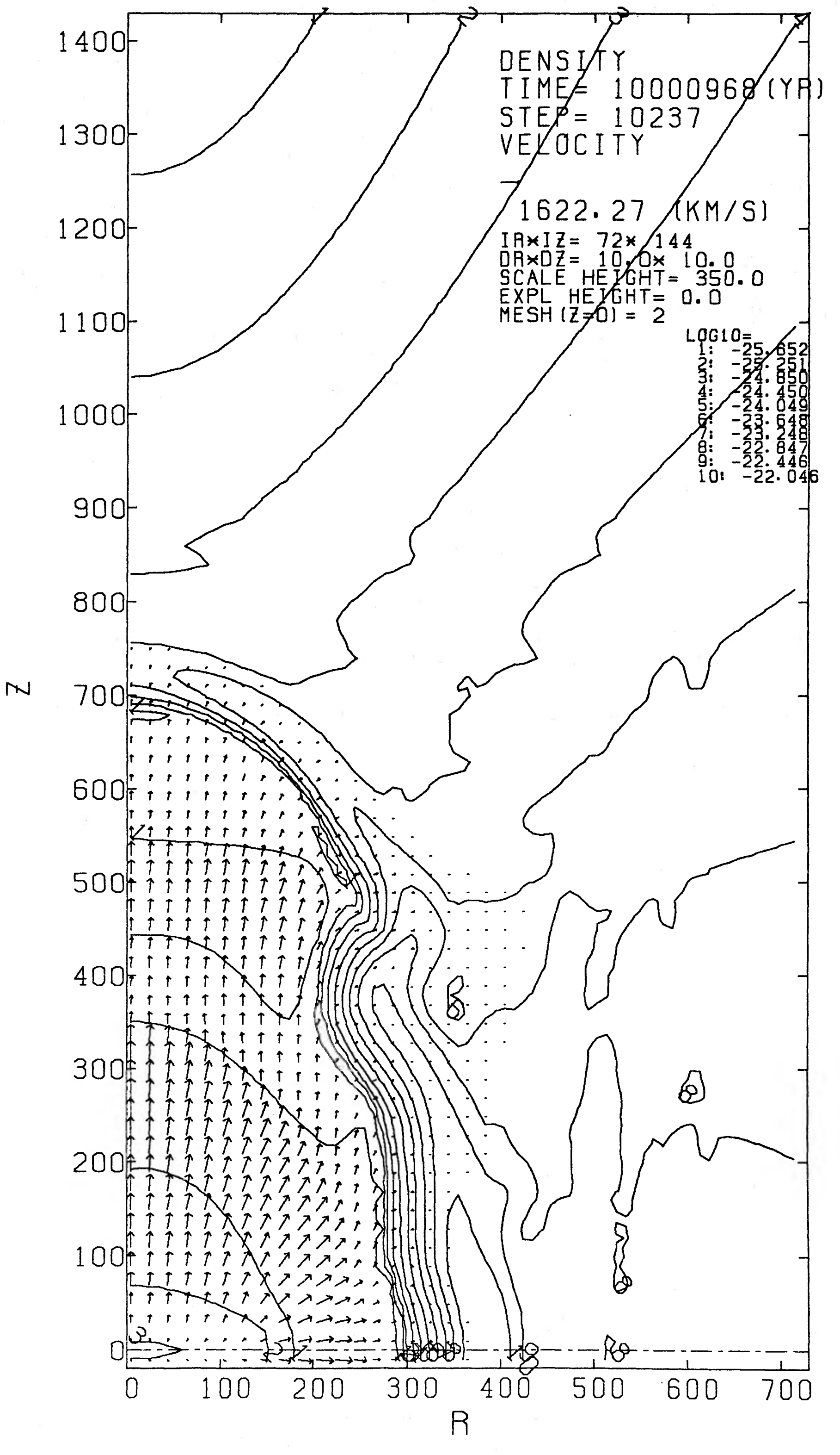

FIG. 9.—Same as in Fig. 2, but for case E ($\Delta t = 200$ yr) at $t = 10^7$ yr. It is clearly seen that in contrast with previous cases the bubble is confined to the disk and does not deform much.

respectively, $n \approx 0.4$ cm^{-3} and $T \approx 3 \times 10^7$ K; although the temperature is the same as that of Case B, the density is higher because of the small size of this bubble. Since the radiative cooling time of the gas with $n \approx 0.4$ cm^{-3} and $T \approx 3 \times 10^7$ K is as long as $\sim 3 \times 10^7$ yr, the radiative cooling in the cavity does not become important in the case of $n_0 \lesssim 100$ cm^{-3}. The qualitative structure of the bubble is essentially the same as that of the younger bubble formed in a lower density.

After the bubble expands over the scale height of the density distribution in the z-direction ($\approx$300 pc) at the age $t \approx 3 \times 10^6$ yr, the bubble begins to elongate gradually. After 7×10^6 yr, the height of the bubble reaches $\sim$1 kpc, as seen in Figure 8*b*. If the active stage of starburst continues at least for $\sim 10^7$ yr, the final structure of the bubble is similar to the smokestack like cases A and B in the high-density disk as $n_0 \approx 100$ cm^{-3}, and the outflowing hot gas goes up to 2 kpc from the disk plane as in Figure 8*c*.

e) The Effect of Supernova Rate

In this subsection, we extend the calculations to see the effect of supernova rate. We examine (1) cases D ($r_{\mathrm{SN}} = 10^{-2}$ SNe yr^{-1}) and *E* ($r_{\mathrm{SN}} = 5 \times 10^{-3}$ SNe yr^{-1}) in contrast with cases A and B ($r_{\mathrm{SN}} = 10^{-1}$ SNe yr^{-1}), and (2) case F ($r_{\mathrm{SN}} = 2 \times 10^{-2}$ SNe yr^{-1}) with case C ($r_{\mathrm{SN}} = 10^{-1}$ SNe yr^{-1}).

In case D, although the expansion is slower than that of cases A and B as is expected, the bubble expands over the scale height, and finally the hot shocked wind material flows up to $z \approx 1.2$ kpc in $t = 9 \times 10^6$ yr, as seen in Figure 5. The flow is qualitatively similar to those of cases A–C, and the structure at $t = 9 \times 10^6$ yr is very similar to that in Figure 8*b* of case C.

On the other hand, since the supernova rate in case E is taken further lower than that of case D, it is found that the hot gas does not flow out to the halo $z \sim 1$ kpc within 10^7 yr. We show the structure at the age $t = 10^7$ yr in Figure 9. Although the bubble elongates a little to the z-direction, the dense shell entirely surrounds the hot cavity, and the hot gas is completely confined within the wall. Even if the activity continues for 10^7 yr and the gas density in the disk plane is as high as $n_0 \approx 20$ cm^{-3}, the hot gas halo up to $z \sim 2$ kpc cannot be formed by the supernova burst when the supernova rate is so low as $r_{\mathrm{SN}} \lesssim (200 \text{ yr})^{-1}$.

In case F, the hot gas cannot be pushed up to the halo $z \sim$ 1–2 kpc in 10^7 yr due to high density ($n_0 = 100$ cm^{-3}) and low supernova rate ($\Delta t = 50$ yr); at the time $t \approx 10^7$ yr the bubble only extends to $z \approx 400$ pc. For both cases D and F, the liberated energy by supernovae is efficiently radiated away from the dense wall and the hot gas within the cavity cannot escape to the halo hindered by the wall. In the parameter space of (n_0, r_{SN}), the region where hot gas halo is formed in $t \approx 10^7$ yr is shown in Figure 10.

f) Comparison with Single Explosion

An intense explosion which occurred $\sim 10^7$ yr ago and continued for a short period $\ll 10^7$ yr may also explain the galactic scale bipolar outflow. To see the difference between the single explosion and the continuous energy injection, we investigate the model that a single explosion with energy $E = 10^{57}$ ergs and ejected mass $M = 10^7$ $M_\odot$ occurs at the center of the disk. The values of the ejected energy and mass correspond to those expected in case A if the supernova explosions continue for 10^7 yr.

The shell cavity structure is also formed. However, the expansion of the shell is faster than case A, because all the energy is injected initially. At the age $t = 10^6$ yr, the shock front reaches upwardly $z \approx 1.3$ kpc. The density and temperature in the cavity are approximately equal to $n \approx 0.4$ cm^{-3} and $T \approx 10^{6-6.5}$ K. Further, the outer shock front propagates to $z \approx 2.7$ kpc at the age

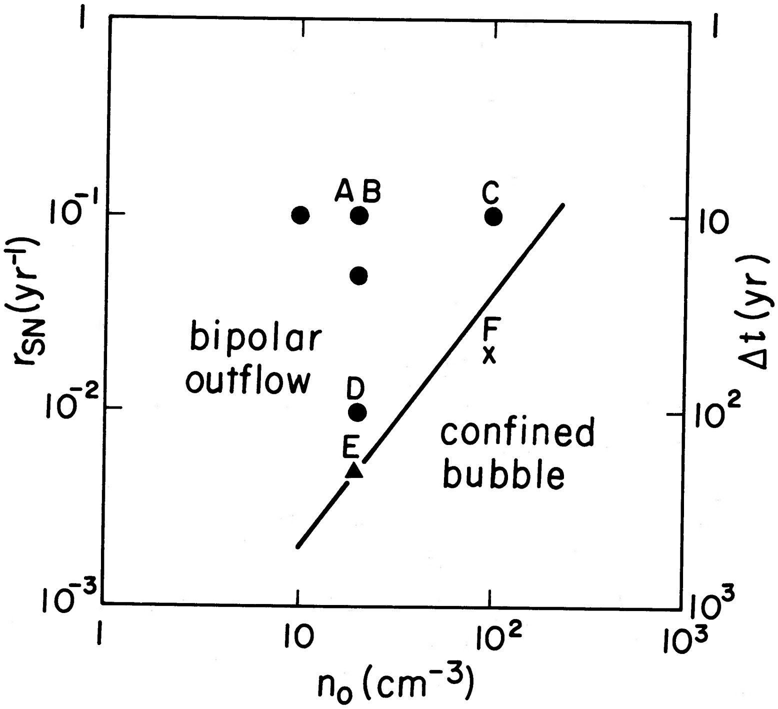

FIG. 10.—Parameter region where the hot gas halo extended to $z \approx 1$ kpc is formed in $t \approx 10^7$ yr

$t = 2.3 \times 10^6$ yr. However, the cavity rapidly cools, because the radiative cooling works effectively in this gas as the cooling time $\lesssim 10^6$ yr as well as the adiabatic cooling. The temperature in the cavity finally decreases to $\sim 10^4$ K.

In consequence, although the single intense explosion can reproduce the size of the bubble as $z \gtrsim 2$ kpc, the temperature in the bubble is too low to explain the X-ray observation. In other words, the existence of the hot matter which emits the thermal X-ray indicates that *the energy source must be now alive in the center of the gas disk.*

IV. DISCUSSION

a) Overall Feature

Figure 11 shows the relation between the expected distribution of the column density of neutral gas and that of the soft X-ray intensity in *Einstein's* HRI band for case B2. The soft X-ray intensity is estimated from the emissivity derived by Raymond, Cox, and Smith (1976). We add the emissivities in three bands (0.284–0.532 keV, 0.532–0.873 keV, 0.873–1.56 keV) and one-half of the emissivity in 1.56–8.265 keV, to substitute for that in *Einstein*'s HRI band (0.2–4 keV), $\Lambda_{\rm HRI}$. Then, if the absorption in the source can be ignored,[1] the surface brightness is given as

$$I_{\rm HRI} = \frac{1}{4\pi} \int \Lambda_{\rm HRI}\, ds \,, \tag{4.1}$$

where the integration is done through the path length for an edge-on galaxy. As seen in Figure 11, the ridge in neutral gas is located just outside the X-ray emission. This agrees with the relative distribution of H_2 in M82 derived by Nakai *et al.* (1987) and X-ray by Watson, Stanger, and Griffiths (1984). Furhter, Lo *et al.* (1987) have pointed out that the 2 μm IR emission, which is radiated by red giants and supergiants, is situated between the peaks of H_2 column density. In our model, a large number of stars are assumed to be distributed near the energy injection region of this flow and the peak of column density is formed just outside it.

These show that the observed gas distribution, i.e., the hot gas is surrounded cylindrically by the cool gas, is well explained by this model. Further, the relation of the energy source and the distribution of gas in numerical simulation is consistent with observation. It is concluded that the starburst nucleus forms the galactic-scale bipolar flow in consequence of the active supernova explosions.

Heckman, Armus, and Miley (1987) have found the large bipolar nebulae associated with powerful ($\sim 10^{12}\ L_\odot$) far-infrared galaxies, Arp 220 and NGC 6240, whose sizes range from ~ 10 to ~ 20 kpc. Although their size is much larger than those examined here, the physical process to form the bipolar outflow seems to be the same.

b) X-Ray Appearance of Hot Halo

By the observation of the HRI on the *Einstein* satellite, the soft X-ray emission extends perpendicularly to the disk of the galaxy up to from 1 kpc (NGC 253; Fabbiano and Trinchieri 1984) to 2–3 kpc (M82; Watson, Stanger, and Griffiths 1984). On the other hand, it extends in the disk plane of 250 pc (NGC 253) to 500 pc (M82) from the center of the galaxy. The observed ratio of the height to the width is almost equal to 4. Our model shown here naturally explains this ratio by the collimation of the originally isotropic flow due to a large density gradient along the rotation axis of the galaxy. The axial ratio of Figure 11 is ~ 4.5.

The observed surface intensity of the HRI band was read from the contour map and was converted to physical units, where we assumed that 1 HRI count $\rm s^{-1}$ is equivalent to 3×10^{-10} ergs $\rm s^{-1}\ cm^{-2}$ (Giacconi *et al.* 1979). For M82, the surface brightness along the minor axis (SE side) gradually decreases from 9.7×10^{-5} ergs $\rm s^{-1}\ cm^{-2}\ sr^{-1}$ at $z \approx 500$ pc to 8.4×10^{-6} ergs $\rm s^{-1}\ cm^{-2}\ sr^{-1}$ at $z \approx 2$ kpc (Kronberg, Biermann, and Schwab 1985). Total luminosity in this band attains $\sim 2 \times 10^{40}$ ergs $\rm s^{-1}$ (Watson, Stanger, and Griffiths 1984).

The total luminosity expected from our model is calculated by integrating the emissivity as

$$L_{\rm HRI} = \iint \Lambda_{\rm HRI}\, \pi r\, dr\, dz \,. \tag{4.2}$$

In Table 1, the X-ray luminosity obtained by the numerical simulation is summarized. It is shown that the luminosity of $\sim 2 \times 10^{40}$ ergs $\rm s^{-1}$ is emitted in cases A–C, but in cases D–F the total luminosity is only $\sim 10^{39}$ ergs $\rm s^{-1}$. This means that a supernova rate higher than $\sim 0.1\ \rm yr^{-1}$ or a mechanical luminosity more than $\sim 3 \times 10^{42}$ ergs $\rm s^{-1}$ is necessary to explain the observed X-ray luminosity.

In Figure 12, we illustrate the profile of the X-ray intensity along the z-axis for cases B2, C, and C2. We also plot the data of intensity observed in M82 and NGC 253. From Figure 12, it is found that the X-ray intensity from the free wind region decreases rapidly. This is understood as follows: because the gas flow in the free wind region is almost radial, the density decreases as $\rho \propto z^{-2}$, and the temperature decreases as $T \propto z^{-4/3}$ due to adiabatic cooling. Thus, the surface brightness of free-free emission is proportional to $T^{1/2}\rho^2 z \propto z^{-11/3}$. In contrast, the surface brightness of the shocked wind region is nearly constant or even increases with increasing z. Observed $I_{\rm HRI}$ decreases from $z = 500$ pc to $z = 2$ kpc by only 1/10; this fact fits well to our model calculation, although the expected surface brightness is smaller than that observed. In conclusion, the X-ray flux observed at low z is originated in the free wind region and that at high z is in the shocked wind matter.

---

[1] Since the H_2 column density in the disk of M82 has been reported as $N_{H_2} \approx (2\text{–}3) \times 10^{22}\ \rm cm^{-2}$ (Nakai *et al.* 1987; Lo *et al.* 1987), the X-ray seems to experience much absorption. But the surface filling factor is estimated as small as ~ 0.25 by Nakai *et al.* (1987). Therefore, the remaining 75% of the emitted X-ray is transported without much absorption, and we do not take the effect of absorption into account here.

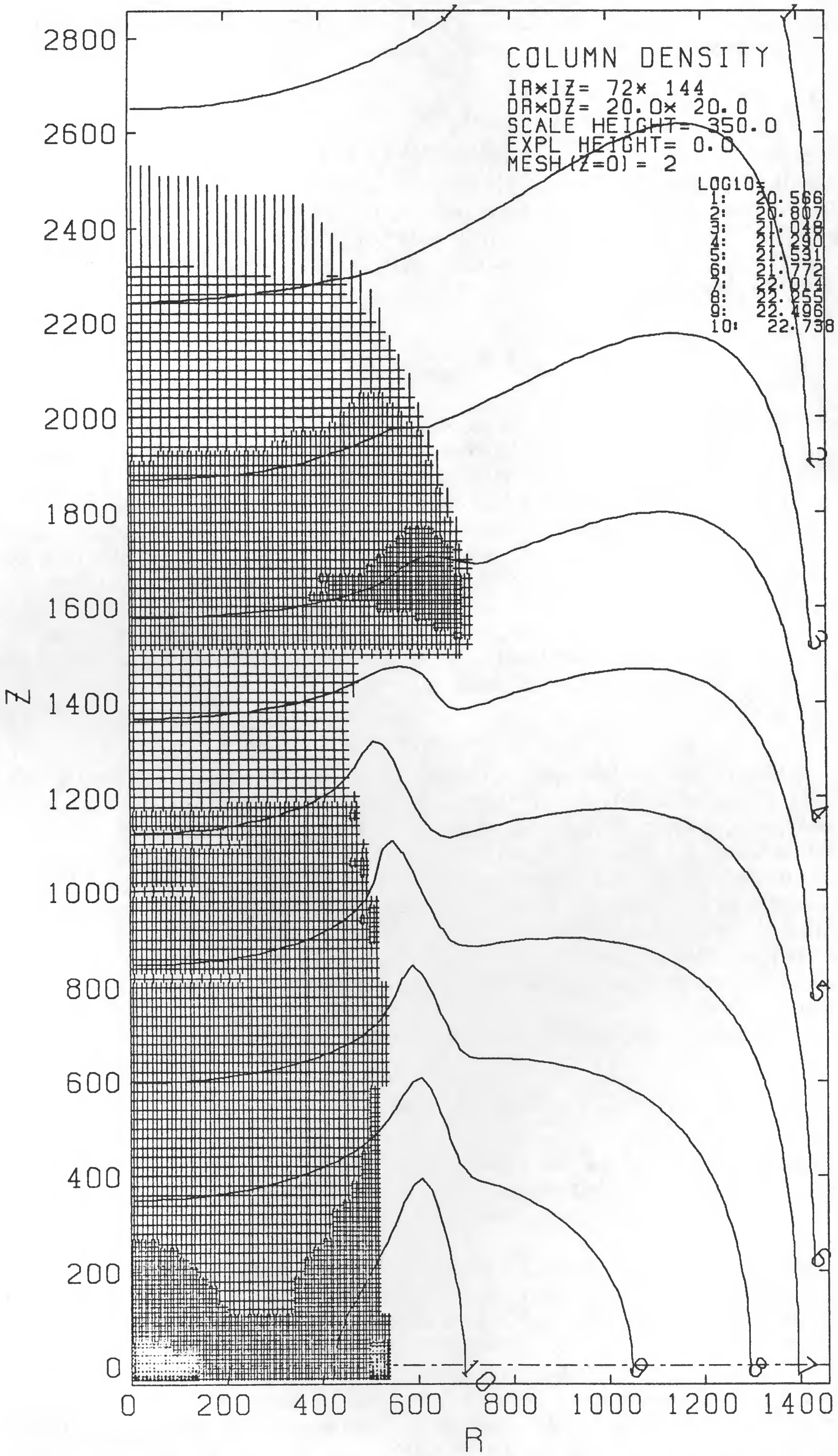

FIG. 11.—Column density of neutral gas and the soft X-ray intensity for the case shown in Fig. 6. The column density of neutral gas is illustrated in contour lines. On the other hand, the X-ray surface brightness is shown in gray-scale representation. The region bright in soft X-ray is surrounded by neutral gas spur like a wall of a funnel.

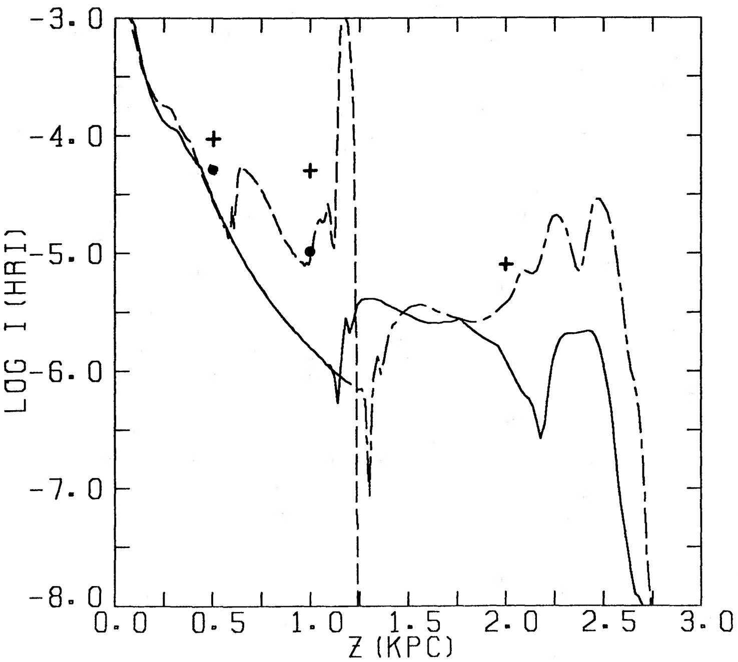

FIG. 12.—Profile of the X-ray intensity in HRI band along the z-axis for cases B2 (*solid line*), C (*dashed line*), and C2 (*dash-dotted line*). We also plot the observational data of M82 (*cross*) and NGC 253 (*circle*).

We would like to acknowledge Professor S. Sakashita and H. Hanami for fruitful discussion on the bipolar outflow and N. Nakai for discussion on starburst galaxies. The numerical calculations were performed by FACOM M380-R at Tokyo Astronomical Observatory, HITAC S810/M680-H at Computer Center, University of Tokyo, and FACOM VP100 at Institute of Space and Astronautical Sciences. This work was supported in part by Grant-in-Aid for Encouragement of Young Scientist from the Ministry of Education, Science and Culture (61790072). One of us (K. T.) also acknowledges the JSPS Fellowships for Japanese Junior Scientists for financial aid in fiscal years 1986 and 1987.

REFERENCES

Beck, S. C., Lacy, J. H., Baas, F., and Townes, C. H. 1978, *Ap. J.*, **226**, 545.
Chevalier, R. A., and Clegg, A. W. 1985, *Nature*, **317**, 44.
Dietz, R. D., Smith, J., Hackwell, J. A., Gehrz, R. D., and Grasdalen, G. L. 1986, *A.J.*, **91**, 758.
Fabbiano, G., and Trinchieri, G. 1984, *Ap. J.*, **286**, 497.
Giacconi, R., *et al.* 1979, *Ap. J.*, **230**, 540.
Heckman, T. H., Armus, L., and Miley, G. K. 1987, *A.J.*, **93**, 276.
Ikeuchi, S. 1978, *Pub. Astr. Soc. Japan*, **30**, 563.
Kronberg, P. P., Biermann, P., and Schwab, F. R. 1985, *Ap. J.*, **291**, 693.
Kronberg, P. P., and Sramek, R. A. 1985, *Science*, **227**, 28.
Lapidus, A. 1967, *J. Comput. Phys.*, **2**, 154.
Lo, K. Y., Cheung, K. W., Masson, C. R., Phillips, T. G., Scott, S. L., and Woody, D. P. 1987, *Ap. J.*, **312**, 574.
MacCormack, R. W. 1971, in *Lecture Notes in Physics*, Vol. **8**, *on Numerical Methods in Fluid Dynamics*, ed. M. Hold (Berlin: Springer), p. 151.
Morita, K. 1982, *Pub. Astr. Soc. Japan*, **34**, 65.
Nakai, N. 1986, Ph. D. thesis, University of Tokyo.
Nakai, N., Hayashi, M., Handa, T., Sofue, Y, Hasegawa, T., and Sasaki, M. 1987, *Pub. Astr. Soc. Japan*, **37**, 685.
Norman, M. L., Winkler, K.-H. A., and Smarr, L. L. 1983, in *Astrophysical Jets*, ed. A. Ferrari and A. G. Pacholczyk (Dordrecht: Reidel), p. 227.
Olofsson, H., and Rydbeck, G. 1984, *Astr. Ap.*, **136**, 17.
Raymond, J. C., Cox, D. P., and Smith, B. W. 1976, *Ap. J.*, **204**, 290.
Rieke, G. H., Lebofsky, M. J., Thompson, R. I., Low, F. J., and Tokunaga, A. T. 1980, *Ap. J.*, **238**, 24.
Różyszka, M., and Tenorio-Tagle, G. 1985, *Astr. Ap.*, **147**, 209.
Salpeter, E. E. 1955, *Ap. J.*, **121**, 161.
Tammann, G. A., and Sandage, A. 1968, *Ap. J.*, **151**, 825.
Tassoul, J.-L. 1978, *Theory of Rotating Stars* (Princeton: Princeton University Press).
Telesco, C. M., and Harper, D. A. 1980, *Ap. J.*, **235**, 392.
Tinslay, B. M. 1972, *Astr. Ap.*, **20**, 383.
Tomisaka, K., Habe, A., and Ikeuchi, S. 1981, *Ap. Space Sci.* **78**, 273.
Tomisaka, K., and Ikeuchi, S. 1986, *Pub. Astr. Soc. Japan*, **38**, 697.
Turner, J. L., and Ho, P. T. P. 1985, *Ap. J.* (*Letters*), **299**, L77.
Ulrich, M.-H. 1978, *Ap. J.*, **219**, 424.
Unger, S. W., Pedlar, A., Axon, D. J., Wilkinson, P. N., and Appleton, P. N. 1984, *M.N.R.A.S.*, **211**, 783.
Watson, M. G., Stanger, V., and Griffiths, R. E. 1984, *Ap. J.*, **286**, 144.
Weaver, R., McCray, R., Castor, J., Shapiro, P., and Moore, R. 1977, *Ap. J.*, **218**, 377.
Wynn-Williams, C. G., Becklin, E. E., Matthews, K., and Neugebauer, G. 1979, *M.N.R.A.S.*, **189**, 163.

SATORU IKEUCHI and KOHJI TOMISAKA: Tokyo Astronomical Observatory, University of Tokyo, Mitaka, Tokyo 181, Japan